

Study of the sensitivity of a solar axion search experiment using SOI pixel detector

Tatsuki Ose

Department of Physics, The University of Tokyo

January 12, 2018

Abstract

A solar axion search experiment is planned to perform. The axions would be produced when thermally excited ^{57}Fe in the Sun relaxes to its ground state and could be detected via resonant excitation of the same nuclide in a laboratory. This experiment expects to catch the 14.4-keV γ -ray which the nuclide absorbing axions emits when deexcited. As the γ -ray detector, the SOI pixel sensor can be used and the XRPIX, the SOI pixel sensor for X-rays, is studied. In this thesis, we discuss the estimation of the sensitivity of the experiment using the XRPIX. Firstly, the radioactive sources in the internal components of the experimental setup was measured by using the HPGe and the G10 chip board itself was found to contain the largest amount of the radioactive sources. Using this result, the background events in the axion search experiment was simulated by Geant4. It was found that the 13.5-keV peak caused from ^{228}Ra in the ^{232}Th series appears near the signal peak. The sensitivity for the one month measurement was estimated by using the maximum likelihood method and the Feldman-Cousins approach for the obtained MC data. The upper limit of the axion mass is estimated as $m_a < 104$ eV at the 95% confidence level. There is room to improve the sensitivity in the pilot experiment and the low background setup is being developed.

Acknowledgements

I would like to express the deepest appreciation to Prof. Hiroaki Aihara for giving an opportunity to research in high energy physics. I am also deeply grateful to Dr. Yoshiyuki Onuki for supporting my studies and encouraging me, to Alejandro Mora for making the clustering system and improving the English sentences I wrote.

I owe a very important debt to the XRPIX group, Prof. Yasuo Arai, Prof. Takeshi Tsuru, Dr. Ayaki Takeda for the development of XRPIXs and the supervision of my studies. I would like to express my gratitude to Dr. Yoshizumi Inoue for teaching me the axion physics and the measurement of the radioactivity of the chip board components, Dr. Yoshio Kamiya for the help of the alpha-ray measurements.

I would like to thank the members of Aihara-Yokoyama group for gaining lots of experiences and the enjoyable life, Kumiko Kono for the greatest supports.

Finally, I would like to express my gratitude to my parents for continuously supporting me.

Contents

1	Introduction	5
1.1	The Strong <i>CP</i> Problem	5
1.2	The Axion	7
1.3	The Hadronic Solar Axions and the Conversion Mechanism in ^{57}Fe . . .	10
2	Experimental Setup	15
2.1	The SOI Pixel Detector	15
2.1.1	The SOI Pixel Detector	15
2.1.2	XRPIX Series	15
2.2	Setup of Background Study	16
2.3	Setup of Pilot Experiment	18
3	Data Analysis	22
3.1	Analysis Flow	22
3.1.1	Offset Subtraction	23
3.1.2	Hit Pixel Selection	23
3.1.3	Clustering	23
3.1.4	Event Selection	24
3.1.5	Energy Calibration	25
3.2	Source Test	25
3.3	Background Measurement	28
4	Detector Background Simulation	30
4.1	Simulation Scheme	30
4.2	Chip Board Components	30
4.3	Geant4 MC Simulation	34
4.3.1	Detector Setup	34
4.3.2	Particle Generation	34
4.3.3	Result	35

5	Sensitivity Estimation	38
5.1	Detection Efficiency for 14.4 keV γ -ray	38
5.2	Signal Fitting Test	38
5.2.1	Likelihood Function and the Best Fit	39
5.2.2	Confidence Interval	40
5.3	Mass Limit	41
6	Discussion and Future Prospects	43
6.1	Estimations under Other Conditions	43
6.2	Comparison with Other Experiments	44
6.3	Developments for Low Background	45
6.4	Goal of Axion Search	46
7	Conclusion	47
A	Background Measurement using the CdTe Detector	51
B	Analysis of Radioactive Impurity Data Taken with the HPGe	54
C	Geant4 Simulation Method	56

Chapter 1

Introduction

Particle Physics deals the nature of all matter in the universe and has discovered many particles. In 2012, when the Higgs boson was found, all parts of the Standard Model Theory fell into place. However, there are still many phenomena which fail to explain by the Standard Model. The existence of dark matter, the matter-antimatter asymmetry of the Universe, and so on. To figure them out, a lot of hypotheses should be prepared and tested experimentally. “Axion” is one of the keys to the undiscovered physics.

We introduce “The Strong CP Problem” and the solution proposed by Peccei and Quinn. The solution predicts an existence of an additional pseudo-scalar particle, called the axion. Then after, we mention the Hadronic Solar Axion as a motivation of this study.

1.1 The Strong CP Problem

Consider the QCD Lagrangian density. Requiring the Lagrangian density to be invariant under transformations of the $SU(3)$ group, we obtain

$$\mathcal{L}_{QCD} = -\frac{1}{4}G_{\mu\nu}^a G^{a\mu\nu} + \bar{\Psi} (i\not{D} - m) \Psi \quad (1.1)$$

$$G_{\mu\nu}^a = \partial_\mu A_\nu^a - \partial_\nu A_\mu^a + g_s f_{abc} A_\mu^b A_\nu^c, \quad (1.2)$$

where A_μ^a is a $SU(3)$ Gauge field and in this case it corresponds to the gluon field, g_s is the coupling constant of strong interactions, f_{abc} are the structure constants of $SU(3)$ and a is the index of the eight gluons.

The first term in (1.1) corresponds to the kinetic energy of the physical gluon field. The second term indicates the interactions between quarks and gluons and the mass term of quarks, which is given by the Higgs structure in the electroweak interaction. However,

there is a term;

$$\mathcal{L}_\theta = \theta \frac{g_s^2}{16\pi^2} \tilde{G}_{\mu\nu}^a G^{a\mu\nu} \quad (1.3)$$

$$\tilde{G}_{\mu\nu}^a = \frac{1}{2} \epsilon_{\mu\nu\rho\sigma} G^{\rho\sigma} \quad (1.4)$$

which can be added to this Lagrangian density and is invariant under transformations of the $SU(3)$ group too. This term is caused by the so-called θ -vacuum. θ is a free parameter.

If we assume that the quarks are massless, the QCD Lagrangian is invariant under chiral transformations. Thus, the axial current J_5^μ

$$\partial_\mu J_5^\mu = \partial_\mu (\bar{\Psi} \gamma^\mu \gamma^5 \Psi) = 0$$

exists and an axial charge Q_5

$$Q_5 = \int J_5^0(x) d^3x \quad (1.5)$$

can be defined as a conserved quantity. Considering quantum corrections, however, J_5^μ is not conserved because of the loop effect of the triangle diagram (see Figure 1.1). This chiral anomaly generally appears when an axial current combines with other two axial currents or two polar currents. The effect of the gluon field combination is

$$\partial_\mu J_5^\mu = 2n_f \frac{g_s^2}{16\pi^2} \tilde{G}_{\mu\nu}^a G^{a\mu\nu}, \quad (1.6)$$

where n_f is the number of fermions. The variation of the Lagrangian in local chiral transformations, $\delta\Psi = -i\delta\alpha\gamma^5\Psi$, is

$$\delta\mathcal{L} = \delta\alpha\partial_\mu J_5^\mu = \delta\alpha 2n_f \frac{g_s^2}{16\pi^2} \tilde{G}_{\mu\nu}^a G^{a\mu\nu} \quad (1.7)$$

and this implies that the θ in (1.3) changes to $\theta + 2\alpha n_f$ under chiral transformations, $\Psi \rightarrow e^{i\alpha\gamma^5}\Psi$.

The mass term itself also breaks the axial current conservation and its effect on whole Lagrangian has the same form as (1.3). So this contribution is considered to be included in θ of (1.3). The effects of θ -vacuum and quarks' masses are considered to be completely independent so there is no reason to cancel out each other. Therefore, \mathcal{L}_θ is thought generally not to be zero.

The term of \mathcal{L}_θ violates P -symmetry and T -symmetry, but conserves C -symmetry. Thus, it causes CP violation. When $\mathcal{L}_\theta \neq 0$, this factor contributes to the electric dipole moment of neutrons d_n . According to calculations,

$$d_n \sim 3 \times 10^{-16} \theta e \text{ cm}, \quad (1.8)$$

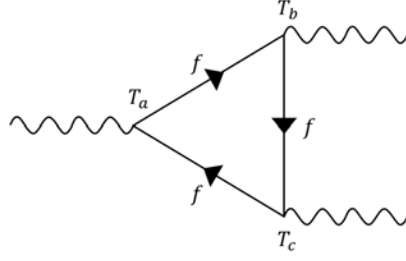


Figure 1.1: Triangle diagram. Three kinds of currents are combined with the loop made of fermions.

but the experimental upper limit is $d_n < 2.9 \times 10^{-26} e \text{ cm}$ [1], which corresponds to $\theta \lesssim 10^{-10}$. This mystery of why the value of theta is so small when there is no reason for it to be so is known as the “Strong CP problem.”

1.2 The Axion

If more than one of the quarks were massless, an extra degree of freedom in the chiral transformation would allow us to set $\theta = 0$. However, some low-energy phenomenology shows the lightest quark must have the limited mass. Another solution is the introduction of new symmetry, called PQ symmetry, first proposed by Peccei-Quinn [2].

We consider especially the up quark (u) and the down quark (d). The Yukawa interaction between fermions and the Higgs in the Standard Model is

$$\mathcal{L}_m = \frac{\bar{2}m_u}{v_1} \bar{\Psi}_L \phi_1 u_R + \frac{\bar{2}m_d}{v_2} \bar{\Psi}_L \phi_2 d_R + \text{h.c.} \quad (1.9)$$

To make (1.9) invariant under the chiral transformation, $\phi_{1,2}$ should absorb the phase change of u and d , such as

$$\Psi_L \rightarrow e^{-i\alpha_L} \Psi_L \quad (1.10)$$

$$u_R \rightarrow e^{-i\alpha_{uR}} u_R, \quad d_R \rightarrow e^{-i\alpha_{dR}} d_R. \quad (1.11)$$

To satisfy this, $\phi_{1,2}$ must have the chiral charge Q_5 like quarks and transform under the PQ chiral transformation as

$$\phi_k \rightarrow e^{+i\alpha_k} \phi_k \quad (1.12)$$

$$\alpha_1 = -\alpha_L + \alpha_{uR}, \quad \alpha_2 = -\alpha_L + \alpha_{dR}. \quad (1.13)$$

In short, PQ symmetry requires for the Higgs scalars to change under chiral phase transformations. Establishing PQ symmetry needs at least two independent Higgs

doublets. In order to avoid absorbing the chiral charge part of ϕ_i in the neutral current Z^μ in spontaneous symmetry breaking like the hypercharge part, the chiral charge part should be separated from the hypercharge part. This chiral charge part is the axion. In standard 2-Higgs model without PQ symmetry, this part is the neutral Higgs part A and its form is

$$A \sim -\text{Im}(\phi_1^c)^0 \frac{v_2}{v} + \text{Im}\phi_2^0 \frac{v_1}{v}, \quad v = \sqrt{v_1^2 + v_2^2}, \quad (1.14)$$

where v_i is the vacuum expectation of ϕ_i . In this case that ϕ_i has a certain vacuum expectation, this part can be separated from the other parts and the form is

$$\begin{aligned} \phi_1 &= \frac{1}{2}v_1 \exp(iax/v) \begin{bmatrix} 1 \\ 0 \end{bmatrix} \\ \phi_2 &= \frac{1}{2}v_2 \exp(ia/xv) \begin{bmatrix} 0 \\ 1 \end{bmatrix} \\ x &= v_2/v_1, \end{aligned} \quad (1.15)$$

and the PQ transformation of (1.12) in this case is written as

$$a \rightarrow a + \alpha v. \quad (1.16)$$

The values of Q_5 for fermions depends on the models. According to the original theory, the left-handed fermions f_L have $Q_5 = 0$ and u_R is combined only with ϕ_1 and d_R is with ϕ_2 , and we can set as $\alpha_{u_R} = \alpha x$, $\alpha_{d_R} = \alpha/x$. The current of the chiral symmetry $U_A(1)$ carrying the Q_5 charge is

$$J_{PQ}^\mu = -v\partial^\mu a + x\bar{u}_R\gamma^\mu u_R + (1/x)\bar{d}_R\gamma^\mu d_R. \quad (1.17)$$

This current has color anomaly,

$$\partial_\mu J_{PQ}^\mu = \left(x + \frac{1}{x}\right) \frac{g_s^2}{16\pi^2} \tilde{G}_{\mu\nu}^a G^{a\mu\nu}. \quad (1.18)$$

To examine the relation between the axion and \mathcal{L}_θ , transformation that the axion is deleted formally in Lagrangian is needed. Fermions transform like

$$u_R \rightarrow e^{-iax/v} u_R, \quad d_R \rightarrow e^{ia/xv} d_R. \quad (1.19)$$

After this transformation, the phase

$$\frac{a}{v} \left(x + \frac{1}{x}\right) \equiv \frac{a}{v} N \quad (1.20)$$

is introduced in the mass term and it has the same effect as if θ in \mathcal{L}_θ would be transformed by $\theta + (a/v)N$. N is a coefficient which is different for each model. The excitation of a starts not from 0 but from the stationary point which make its potential the smallest. Therefore,

$$a = a + a_{phys}, \quad \theta + \frac{a}{v}N = 0, \quad (1.21)$$

where a_{phys} is the axion which is observable physically. This result means that the color anomaly gives the Higgs potential extra contributions, the horizontal W-shaped rotational potential leans, and the axion field moves toward the lowest point of potential which is newly generated. Thus, if axions exist, the Higgs field is realigned in order to minimize the vacuum and mechanical factors certify $\theta = 0$.

Summarizing these contributions, the axion Lagrangian \mathcal{L}_a is

$$\begin{aligned} \mathcal{L}_a = & \frac{1}{2} \partial_\mu a_{phys} \partial^\mu a_{phys} \\ & + \frac{1}{v} \left[\partial_\mu a_{phys} \sum_i \left(x \bar{u}_{iR} \gamma^\mu u_{iR} + \frac{1}{x} \bar{d}_{iR} \gamma^\mu d_{iR} \right) + N a_{phys} \frac{g_s^2}{16\pi^2} \tilde{G}_{\mu\nu}^a G^{a\mu\nu} \right] \\ & + \frac{1}{v} \left[\partial_\mu a_{phys} \frac{1}{x} \sum_i \bar{l}_{iR} \gamma^\mu l_{iR} + E a_{phys} \frac{e^2}{32\pi^2} \tilde{B}_{\mu\nu} B^{\mu\nu} \right] \end{aligned} \quad (1.22)$$

$$B^{\mu\nu} = F_{EM}^{\mu\nu} - \tan \theta_W F_Z^{\mu\nu} \quad (1.23)$$

$$N = N_g \left(x + \frac{1}{x} \right), \quad E = 2N_g \left(\frac{4}{3}x + \frac{1}{3x} + \frac{1}{x} \right) \quad (1.24)$$

where N_g is the generation number, $B^{\mu\nu}$ is the $U(1)$ gauge tensor, θ_W is the Weinberg angle, N and E is the values depending on the models. The axion obtains its mass through the chiral anomaly. The axion mass m_a is can be expressed as

$$m_a = \frac{F_\pi m_\pi}{f_a} \sqrt{\frac{m_u m_d}{(m_u + m_d)^2}}, \quad f_a = \frac{v}{N} \quad (1.25)$$

where F_π and m_π are the pion decay constant and mass. Therefore, m_a can be obtained as

$$m_a \sim \frac{6.2 \times 10^6}{f_a/\text{GeV}} \text{ eV}. \quad (1.26)$$

f_a in (1.25) was thought to be on the same order of magnitude as the one for the electroweak breaking $v_F \sim 250$ GeV. However, this model has been reliably ruled out by many experiments. Then, new axion models for which the scale of f_a is arbitrary were considered. They are named ‘‘invisible axion models.’’ There are two models of

them; one is the KSVZ model [3][4], the other is the DFSZ model [5][6]. The KSVZ model introduces a scalar field σ and a superheavy quark X and only X can possess the PQ charge. In this model, the axion cannot couple with electrons in tree-level as this axion is called ‘‘Hadronic Axion.’’ On the other hand, the DFSZ model introduces extra Higgs fields and a scalar field, which cannot couple with fermions directly but can couple through the Higgs potential.

Figure 1.2 shows the major exclusion ranges of f_a .

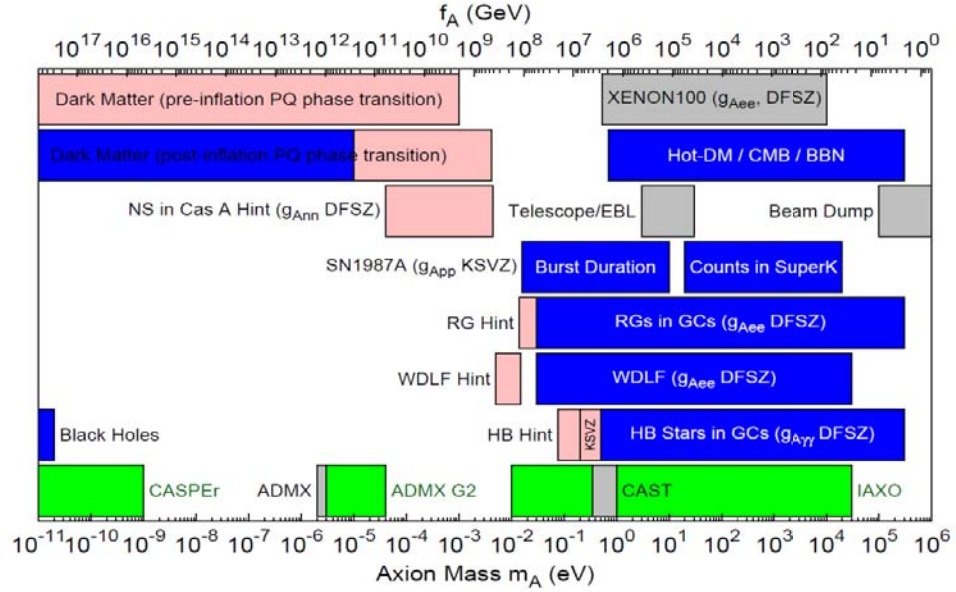


Figure 1.2: Exclusion ranges for m_a (equivalently for f_a .) The blue regions indicate the excluded ones, the pink indicates the hint excluded, the green indicates the projected reach. Limits on coupling strengths are translated into limits on m_a and f_a using $m_u/m_d = 0.56$ and the KSVZ values for the coupling strengths, if not indicated otherwise. Image taken from [7].

1.3 The Hadronic Solar Axions and the Conversion Mechanism in ^{57}Fe

According to the result of SN1987A data [8], it remains a small window in the exclusion ranges of m_a under the KSVZ model (see Figure 1.2), this means that the region, $10 \text{ eV} < m_a < 20 \text{ eV}$, has not been excluded completely. The region is called ‘‘Hadronic Axion Window’’.

1.3. THE HADRONIC SOLAR AXIONS AND THE CONVERSION MECHANISM IN ^{57}Fe 11

Currently, the most popular approaches rely on the axion-two-photon vertex, allowing for axion-photon conversion in external electric or magnetic fields [9]. The interaction between the axion and the two photons is

$$\mathcal{L}_{a\gamma\gamma} = -\frac{1}{4}g_{a\gamma\gamma}a_{phys}F_{\mu\nu}\tilde{F}^{\mu\nu} = g_{a\gamma\gamma}a_{phys}\mathbf{E} \cdot \mathbf{B} \quad (1.27)$$

$$g_{a\gamma\gamma} = \frac{e^2}{8\pi^2 f_a} \left(\frac{E}{N} - 1.92(4) \right), \quad (1.28)$$

where E and N are the electromagnetic and color anomalies of the axial current associated with the axion. If a photon is under a strong, inhomogeneous magnetic field, like inside of the Sun, the photon would be transformed to an axion; this conversion is known as the Primakoff effect [10]. This effect has been widely used to detect solar axion (for example, Tokyo Axion Helioscope [11] and CAST [12]) but this method is strongly dependent on the parameter E and N , which depends on the models.

Another method of searching solar axions was suggested by Moriyama in 1995 [13]. This method does not use the axion-photon coupling but uses the axion-nucleon coupling. If some nuclides in the Sun have magnetic dipole (M1) transitions and are excited thermally, axion emission from nuclear deexcitation would be possible. He suggested to study the M1 transition of ^{57}Fe , since it is one of the stable iron isotopes, and it is exceptionally abundant among heavy elements in the Sun; moreover, the transition energy is 14.4 keV, which would lead to a very distinctive, narrow peak. The whole process is resumed in Figure 1.3.

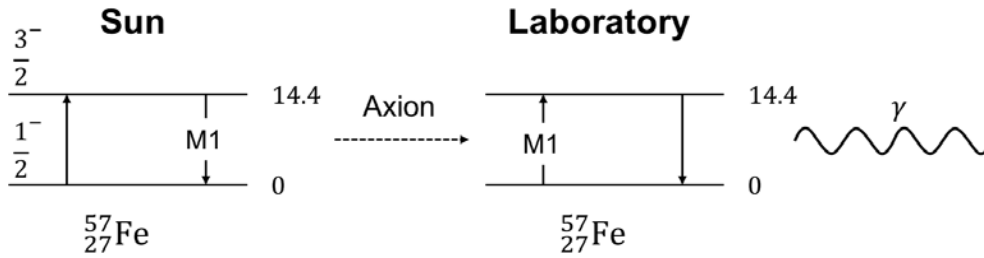


Figure 1.3: Mechanism of axion production and detection. The deexcitation of an iron-57 nucleus in the sun is accompanied by the emission of a 14.4 keV axion, which reaches a piece of the same material —this is, of ^{57}Fe — in the laboratory. The nuclei of iron rise to its first excited level, and in the deexcitation process emits a 14.4 keV photon, which is captured by a detector.

The emission of the axion from ^{57}Fe would be presented using the coupling of

hadronic axions to nucleons, whose interaction term is, following [13],

$$\mathcal{L}_{aNN} = a_{phys} \tilde{N} i \gamma_5 (g_0 + g_3 \tau_3) N \quad (1.29)$$

$$g_0 = -7.8 \times 10^{-8} \left(\frac{6.2 \times 10^6}{f_a/\text{GeV}} \right) \left(\frac{3F - D + 2S}{3} \right) \quad (1.30)$$

$$g_3 = -7.8 \times 10^{-8} \left(\frac{6.2 \times 10^6}{f_a/\text{GeV}} \right) \left[(D + F) \frac{1 - z}{1 + z} \right], \quad (1.31)$$

where D and F denote the reduced matrix elements for the $SU(3)$ octet axial vector currents, S characterizes the flavor singlet coupling and $z = m_u/m_d \sim 0.56$. S involves a big uncertainty and several theories and measurements have reported different values [14][15][16][17].

The differential flux of axions produced by ^{57}Fe , at the energy point $E_s = 14.41$ keV, can be shown in be

$$\Phi_a = 2.0 \times 10^{13} \left(\frac{10^6 \text{GeV}}{f_a} \right)^2 C^2 \text{ cm}^{-2} \text{ s}^{-1} \text{ keV}^{-1} \quad (1.32)$$

$$C \equiv (D + F) \frac{1 - z}{1 + z} - 1.19 \left(\frac{3F - D + 2S}{3} \right) \quad (1.33)$$

and the flux spectrum is shown in Figure 1.4.

The axions coming from the Sun would resonantly excite ^{57}Fe in a laboratory. The rate of the excitation by the ^{57}Fe nucleus is

$$R_a = \frac{\pi}{2} \Phi_a \sigma_{0,a} \Gamma_{\text{tot}} \quad (1.34)$$

$$\sigma_{0,a} = 2\sigma_{0,\gamma} \frac{\Gamma_a}{\Gamma_\gamma}, \quad (1.35)$$

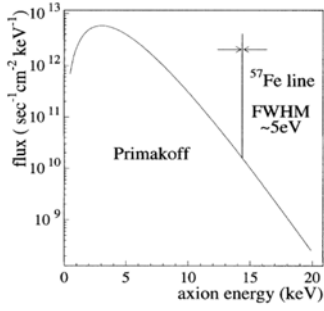
where $\sigma_{0,\gamma} = 2.6 \times 10^{-18} \text{ cm}^2$ is the maximum resonant cross section of γ [18], $\Gamma_{\text{tot}} = 4.7 \times 10^{-12} \text{ keV}$ is the total decay width of the first excited state of ^{57}Fe , and Γ_a/Γ_γ represents the branching ratio of the excited ^{57}Fe state and it was calculated by Haxton and Lee [14] as

$$\frac{\Gamma_a}{\Gamma_\gamma} = \frac{1}{2\pi\alpha} \frac{1}{1 + \delta^2} \left[\frac{g_0\beta + g_3}{(\mu_0 - 1/2)\beta + \mu_3 - \eta} \right]^2, \quad (1.36)$$

where δ is the E2/M1 mixing ratio, μ_0 and μ_3 are the isoscalar and isovector magnetic moments and β and η are the parameters which depend on nuclear matrix elements. The common values for these parameters [13] are summarized in Table 1.1. Using these parameters, the total detection rate per one nucleus of ^{57}Fe in the laboratory is calculated as

$$R_a = 3.3 \times 10^{-28} \left(\frac{10^6 \text{GeV}}{f_a} \right)^4 C^4 \text{ s}^{-1}. \quad (1.37)$$

1.3. THE HADRONIC SOLAR AXIONS AND THE CONVERSION MECHANISM IN ^{57}Fe



Parameter	Value
δ	~ 0
β	-1.19
$\mu_0 - 1/2$	0.38
μ_3	4.71
η	0.80

Table 1.1: Values of parameters used in (1.37) and (1.38).

Figure 1.4: The differential flux of the axion from the Sun. Image is taken from [13].

Derbin's group has done the solar axion search with this method [19]. They employed the values $F = 0.426$, $D = 0.808$ and $S = 0.5$ and derived the expected rate of axion absorption as a function of $(g_0\beta + g_3)$ and m_a ;

$$R_a = \begin{cases} 5.16 \times 10^{-3} (g_0\beta + g_3)^4 & \text{s}^{-1} \\ 9.29 \times 10^{-34} (m_a/\text{eV})^4 & \text{s}^{-1}. \end{cases} \quad (1.38)$$

The axion mass as a function of the expected rate is shown in Figure 1.5. Their experiment reported the upper limit of the axion mass as $m_a \leq 145$ eV at a 95% confidence level.

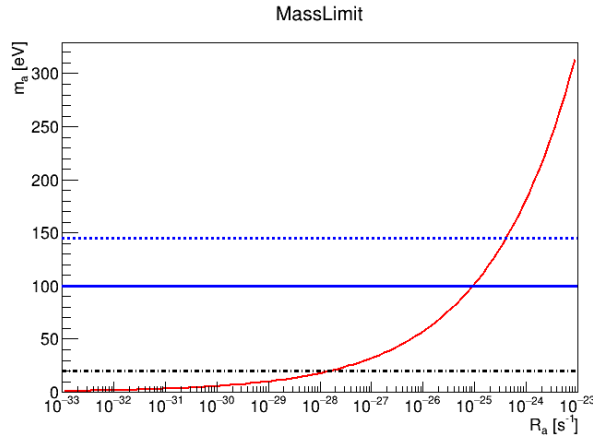


Figure 1.5: The relation between the mass and excited rate. The blue solid line shows the current best limit of the axion mass using the axion-nucleon interactions and the dotted line shows the limit using ^{57}Fe , in particular. The black dashed dotted line shows the upper of ‘‘Hadronic Axion Window’’.

Recently a new SOI pixel detector is being developed and expected to outperform

other existing silicon detectors. This new detector has the possibility of bringing the mass limit down and reaching the non-exclusive mass region.

Chapter 2

Experimental Setup

Here, we describe the experimental setup of searching for the Hadronic Solar Axion introduced in the last chapter. The first section of this chapter will deal with the properties of a silicon pixel detector, which is the core of this setup. The second and third section shows the components of setup which is being used now and plans to be used in the next, respectively.

2.1 The SOI Pixel Detector

2.1.1 The SOI Pixel Detector

A Silicon-On-Insulator (SOI) pixel detector (SOIPIX) has been developing by KEK and other institutes [20]. The SOI wafer is composed of a thick, high resistivity substrate (Sensor), a thin, low resistivity layer (CMOS Circuit), and a buried oxide (BOX) layer (SiO_2 insulator) sandwiched by them (see Figure 2.1). There is no mechanical bump bonding so that higher density, smaller parasitic capacitances, and higher sensitivity than conventional detectors are achievable. Moreover, full CMOS circuitry can be implemented in the pixels. These characteristics make this detector useful for high-energy experiments, astrophysics, medical imaging and so on.

2.1.2 XRPIX Series

XRPIX is one of the SOIPIXs. It is being developed by Kyoto University, Miyazaki University and KEK as a next-generation detector for X-ray astronomy. The biggest feature is that each pixel has its own trigger logic. When radiation hits the sensor, it can output the timing and position information. This gives good timing resolution (less than $10\ \mu\text{s}$) and helps us to do anti-coincidence measurements.

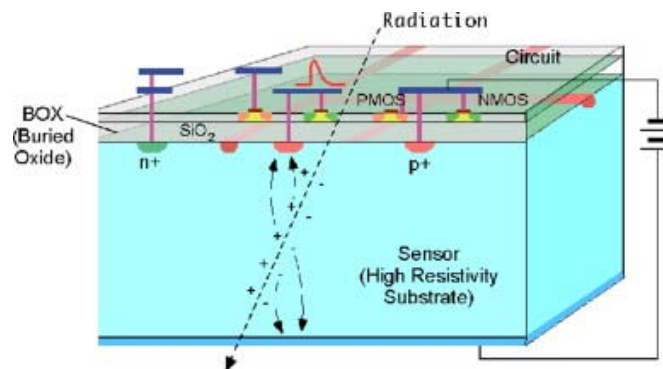


Figure 2.1: The SOI pixel detector[20]

The XRPIX is being improved. In 2010, the first model, XRPIX1, was completed and until now several versions have been produced. The newest version, XRPIX6D, introduced the double-SOI structures and its spectroscopic performance is improved [21]. In this thesis, the XRPIX2b, which is known to work stably, is used for environmental radioactive measurement and the XRPIX5, which is the biggest of the series, is to be used for the pilot experiment of axion search. The chips of the XRPIX2b and the XRPIX5 are shown in Figure 2.2.

The XRPIX has two readout modes basically. One is the frame readout mode, which reads from all pixels at every set time. The other is the event-driven readout mode, which can extract trigger from each pixel and read pixel by pixel.

The pixel circuit of the XRPIX5 is shown in Figure 2.3. In the event-driven readout mode, the pixel whose signal is higher than a threshold, set in the comparator, is judged as a hit pixel. If the signal exceeds the threshold, the comparator transmits the hit trigger to a FPGA controlling the chip and the FPGA starts reading the signal of the hit pixel. We can set the threshold via the FPGA. However, obtaining multiple-pixel-hit events is not available in this readout mode. Thus, we use only frame readout mode in this study.

2.2 Setup of Background Study

The photograph of the whole experimental setup is shown in Figure 2.4. This setup is on the sixth floor of Building No.1 of Faculty of Science, the University of Tokyo. The clean air unit is used to remove the radon contained in the dust. The efficiency of trapping small particles which size is bigger than $0.1 \mu\text{m}$, is more than 99.999%. The thermal chamber can set temperatures from -85°C to 180°C . The size of the inner space is $400 \times 400 \times 400 \text{ mm}^3$. In the inner space, there is a table hanging from the clean booth frame in order to place lead blocks on. There are four holes in the upper side

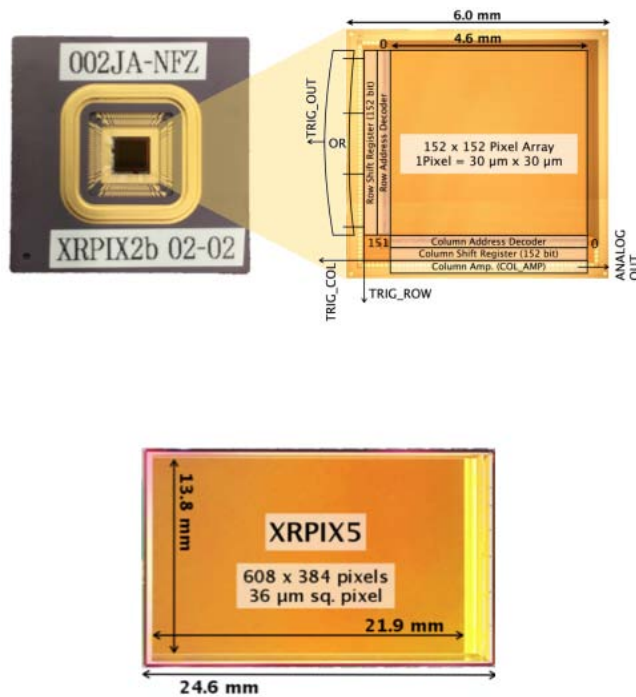


Figure 2.2: Chips of XRPIX. Top is the picture of the XRPIX2b package and the detail of the chip. Bottom is the XRPIX5.

of the chamber through which the table hanging wires and the detector cables pass. The lead blocks were obtained from Minowa group, which was a laboratory in the University of Tokyo and was dissolved as Prof. Minowa retired.

A picture of the XRPIX2b is shown in Figure 2.5. The XRPIX2b is composed of a sub-board and a SEABAS. The chip is provided in the form of a ceramic package. The chip is connected to the package using wire bonding. The sub-board has a socket to mount a chip package on and intermediates between the chip and the SEABAS control. The SEABAS (Soi EvAluation BoArd with Sitcp, [22]) is a universal main board. It contains two Field-Programmable Gate Arrays (FPGAs), one used for chip control and data taking, the other used for data transmission and is responsible for the data conversion and control tasks. It also contains an analog to digital converter (ADC) and a digital to analog converter (DAC) to exchange signals between the chip and the FPGAs. The data is transmitted through an Ethernet cable to DAQ-PC. Originally, the sub-board and the SEABAS can be connected directly through three connectors. A SEABAS conversion board is used when there is no space to put on the SEABAS. Since the conversion board is smaller than the SEABAS, it is used for minimizing the detector space. The conversion board has four D-sub 25 pin connectors.

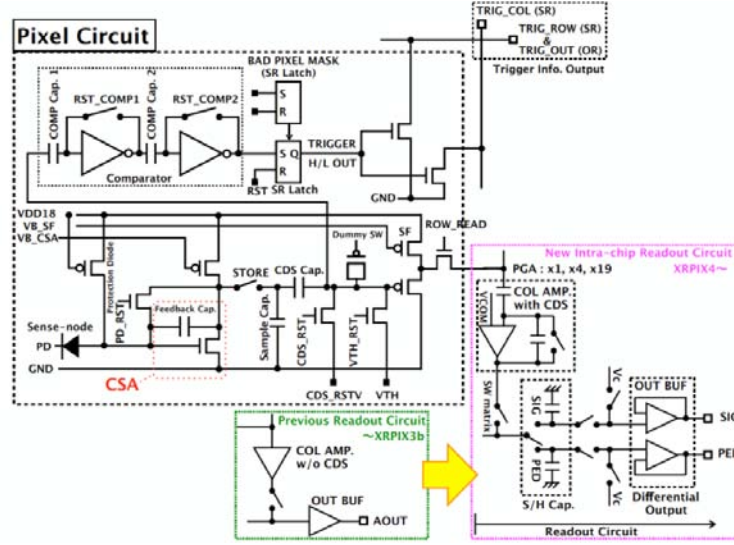


Figure 2.3: The pixel circuit of XRPIX5.

2.3 Setup of Pilot Experiment

Since it is known that the size of the XRPIX2b is not big and we expected poor sensitivity of the axion measurement, the pilot experiment is planned to use the XRPIX5, whose chip is bigger than the XRPIX2b, and a stack-XRPIX system which enables the main board to control multiple chips at the same time.

An image of XRPIX5 stacking setup is shown in Figure 2.6. The stacking module consists of a chip board, Flexible Print Circuit boards (FPCs), a sub-board and the SEABAS. Unlike XRPIX2b, the chip is not packaged but directly implemented and connected by the wire bonding to the chip board. The sub-board has the FPGA which controls the timing synchronization of each module and the serializing readout.

The image of the stacking chip boards and shielding is shown in Figure 2.7. Inside the lead blocks, there are oxygen free copper (OFC) shields to prevent Pb X-rays and γ 's electrons caused by cosmic rays hitting on the lead blocks. The presence of oxygen is less than 0.001%, and copper accounts for at least 99.95% of the material.

The lead and OFC shields are expected to reduce the γ -rays from environmental radioactivity. Moreover, an active shield such as a VETO scintillation counter enables us to make a coincidence with XRPIX and it is expected to reduce cosmic rays related signals.

We measured a background rate with lead and OFC shields using a Cadmium Telluride (CdTe) detector (see Appendix A) and the effect of the shielding materials was studied. The present estimated environmental background rate at 14.4 keV is $\sim 1.23 \times 10^{-3} \text{ h}^{-1} \text{ mm}^{-2} \text{ keV}^{-1}$ under the 15 cm of lead and 20 mm of copper and no

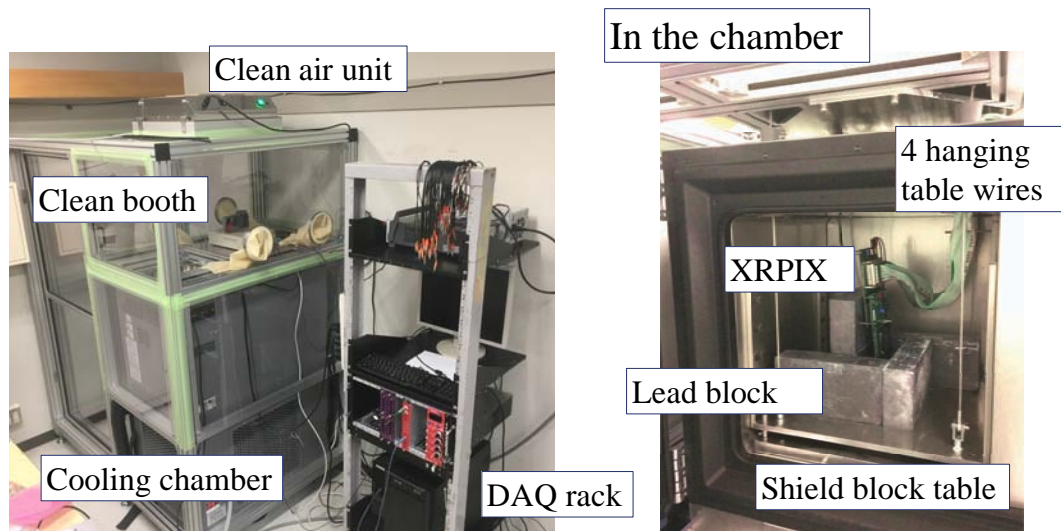


Figure 2.4: The detector construction.

cosmic muons' background [23]. On the other hand, there is a note that the copper shielding should not be thicker than 6 mm in aboveground experiments because muon bremsstrahlung would not stop in the copper. Actually, this measurement shows that the best shielding is the case of the 6 mm thickness in copper, though it may not be significant.

The stacking system is expected not only to increase the detection area but also to reduce the internal background events using the timing coincidence with the different layers of XRPIX stacking. Sequential decays of radioactive nucleus occurring in a very short time can be detected with the different sensors as signal events. These decays happen during the decays of the uranium and the thorium series contained by the parts of the setup. Thus, the multi-hit events can be treated as the non-signal events and removed. Since it is hard for the shielding to reduce the internal background events, this VETO rejection is thought to be essential work.

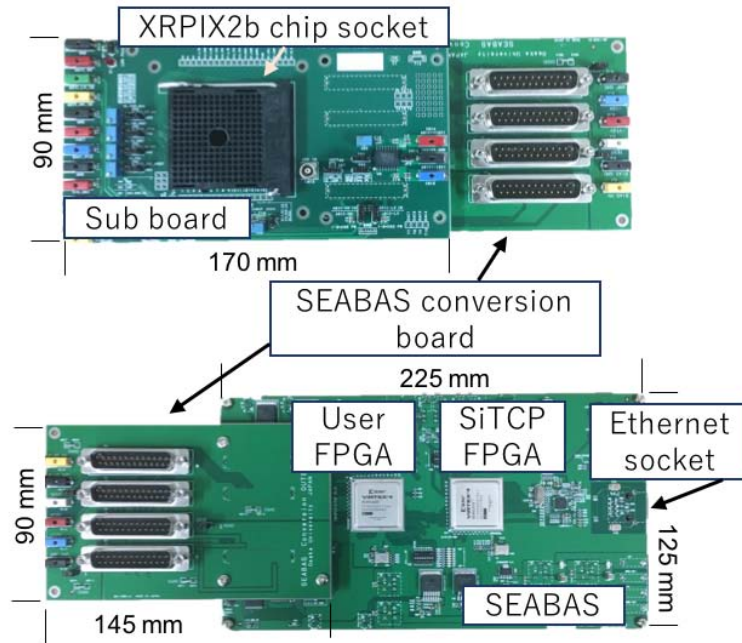


Figure 2.5: XRPIX2b boards.

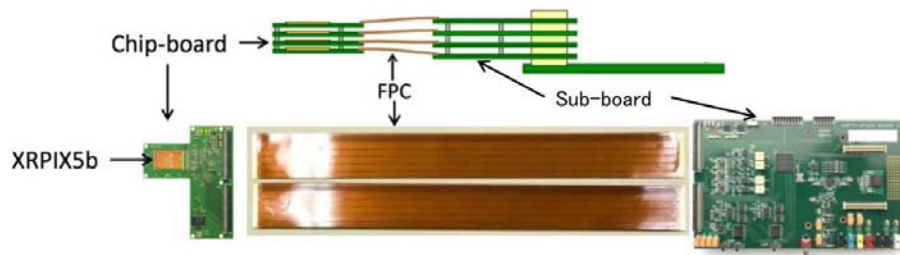


Figure 2.6: The image of stacking boards and connections between these boards.

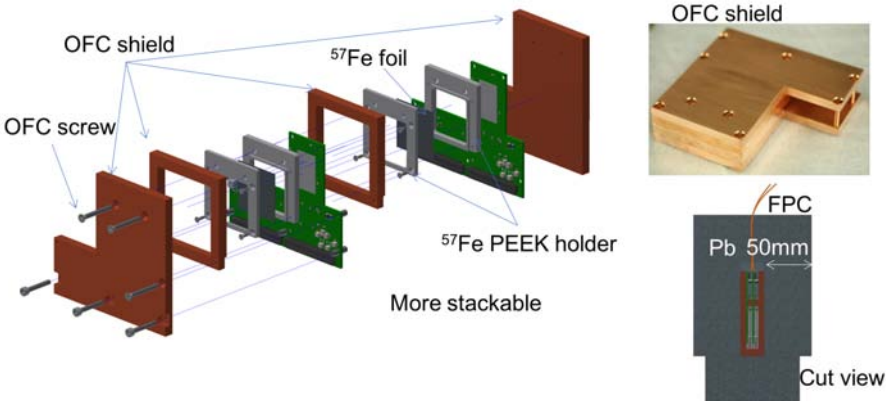


Figure 2.7: The image of chip boards and shielding with lead and OFC.

Chapter 3

Data Analysis

This chapter shows how to analyze the data obtained from XRPIXs and some practical measurements. This study was performed using XRPIX2b and the setup shown in Section 2.2 and aimed to prepare the analysis method for the next pilot experiment with XRPIX5.

3.1 Analysis Flow

The analysis flow of the frame readout mode is shown in Figure 3.1. The frame readout mode reads out charges of each pixel integrated during a fixed time (about 0.1–10 ms). A frame corresponds to all the signals obtained during this time window. After readout, these charges are reset and pixels restart the charge integration. It takes a fixed integration time and about 10 ms as the reading time for every frame cycle.

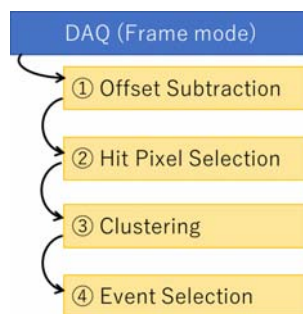


Figure 3.1: Analysis flow from raw data to hit event selection

3.1.1 Offset Subtraction

The frame readout mode obtains the voltage values of all pixels. Since these values contain a offset value, offset subtraction is needed first. The offset has different values from each pixel and varies slightly every second. The offset value at a pixel and a frame is defined as the average value of before and after fifty frames. The process is shown in Figure 3.2. A pulse height (PH) of the pixel is defined by subtracting the offset from the original value.

3.1.2 Hit Pixel Selection

Next, we define the hit pixels in a frame. When the PH of a pixel exceeds a defined threshold, we treated it as the hit pixel. The threshold should be set at far away from the fluctuation of thermal noise. The PH distribution of the pixel in all frames in one data file is fitted with a Gaussian and the pixel in the frame whose PH is five times bigger than the standard deviation σ of the fitted Gaussian is selected as a pixel with a non-zero signal. This process is shown in Figure 3.3.

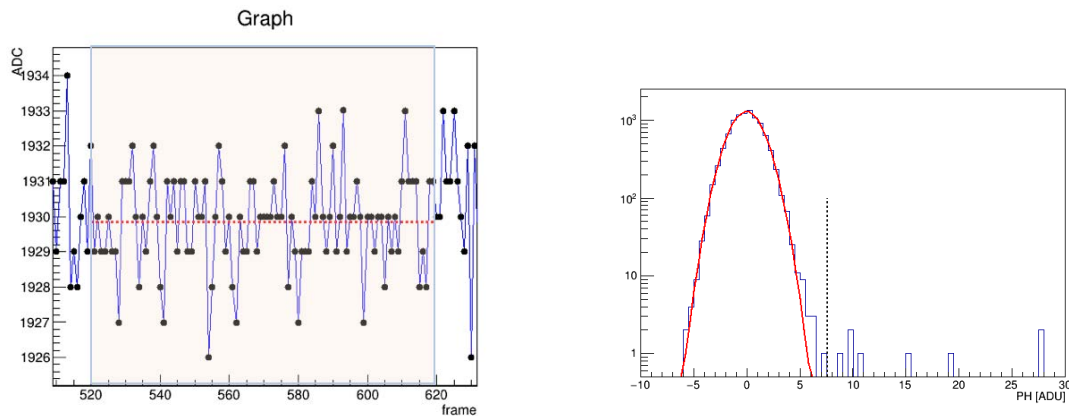


Figure 3.2: Offset subtraction. In this case the offset of frame 570 is the average of the ADC value between frame 520 and 620, shown in the red dotted line.

Figure 3.3: Hit Pixel Selection. The black dotted line shows the threshold of the hit pixel.

3.1.3 Clustering

Some particles hit more than two neighbor pixels at the same time. Such pixels are clustered by the DBSCAN (Density-Based Spatial Clustering of Applications with Noise) algorithm [24] and defined as one cluster event. The cluster events contain some information; the total energy, their size, the number of their rows and columns, geometric

center and signal-weighted center and their linearity. This information gives hints of detected particles. The example of clustering is shown in the next section.

3.1.4 Event Selection

There are bad pixels whose charge fluctuated with some constant value frequently. The example is shown in Figure 3.4. This phenomenon is known to appear in the early XRPIX series and improved in the recent XRPIX series. If such pixel is found, it is defined as a bad pixel and clusters containing bad pixel are removed from event candidates. The definition of the bad pixel is below; the Gaussian function is fitted to the distribution of the PH of a pixel (see the bottom of Figure 3.4), and the least chi-square χ^2 is calculated and divided by the number of degrees of freedom of fitting ν . If the parameter χ^2/ν of the pixel exceeds a certain value (now we defined as 180), the pixel is defined as the bad pixel.

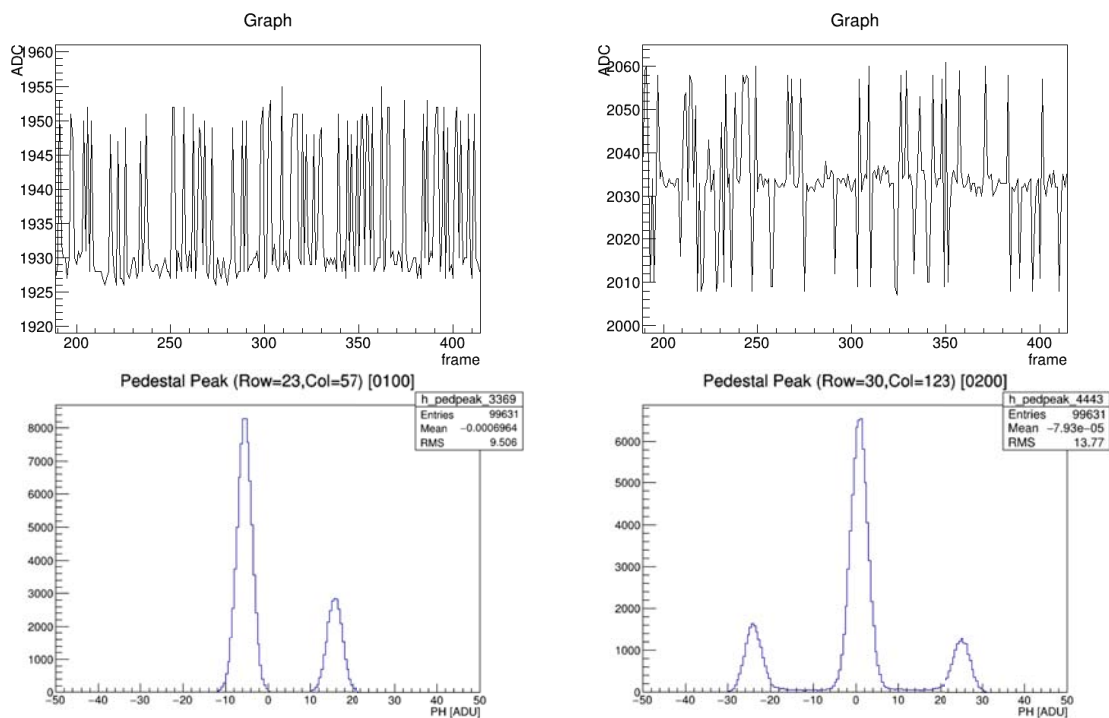


Figure 3.4: The sample of bad pixels. Tops show the charge fluctuation depending on the frames. Bottoms are the distributions of the PH.

Next, border events are removed because their deposited energies fail to sum up and the cluster shapes are not reconstructed correctly. Border events correspond to events occurred near the border of the sensitive area. Its definition is that the cluster contains an edge pixel.

The rest of clusters are treated as event candidates. Using clusters' information, the candidates are assigned for four categories; photons, α particles, electrons and cosmic muons. The details are explained in Ref [25].

3.1.5 Energy Calibration

The obtained voltage values from FPGA are in the form of ADC units. The transformation from ADC units to the energy is done at the beginning of the clustering work. The energy calibration parameters are obtained from an Americium-241 source test, using the peaks of 13.95 keV, 17.7 keV, 20.8 keV, and 26.35 keV. The parameters are slightly changed by the characteristics of chips, temperature, integration time and so on.

3.2 Source Test

A radiation source examination was performed in order to check this analysis flow and the characteristics of each particle obtained by XRPIX. Used sources were Americium-241 for α particles and γ -rays and Strontium-90 for β particles.

The cluster images of them are shown in Figures 3.5 – 3.7. Since α particles deposit a large amount of energy along its short path, a very high density of electron-hole pairs is produced and occurs a charge sharing effect [26]. Thus, α particles are known to shape a circular cluster in the detector. β particles cause multiple scattering in the silicon and the track is struggling. γ -rays leave small pixel clusters.

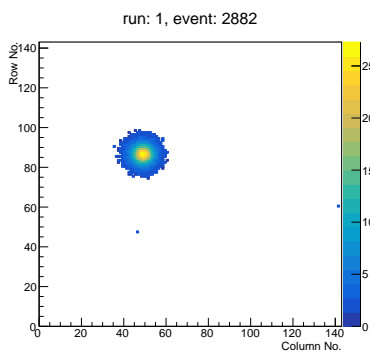


Figure 3.5: Image of an α particle

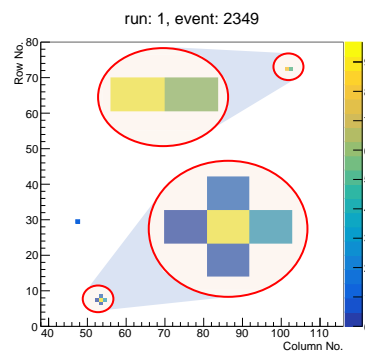


Figure 3.6: Image of γ -rays.

The relevant histograms of the cluster size and the total energy for γ and β are shown in Figure 3.8. In the low energy region, the size of clusters is small for both β and γ because, for example, the range of electrons having 50 keV is about 20 μm , which is smaller than the size of pixels in sensor. The low energy electrons seem to be undistinguishable from photons. However, such an electron having the energy to be able

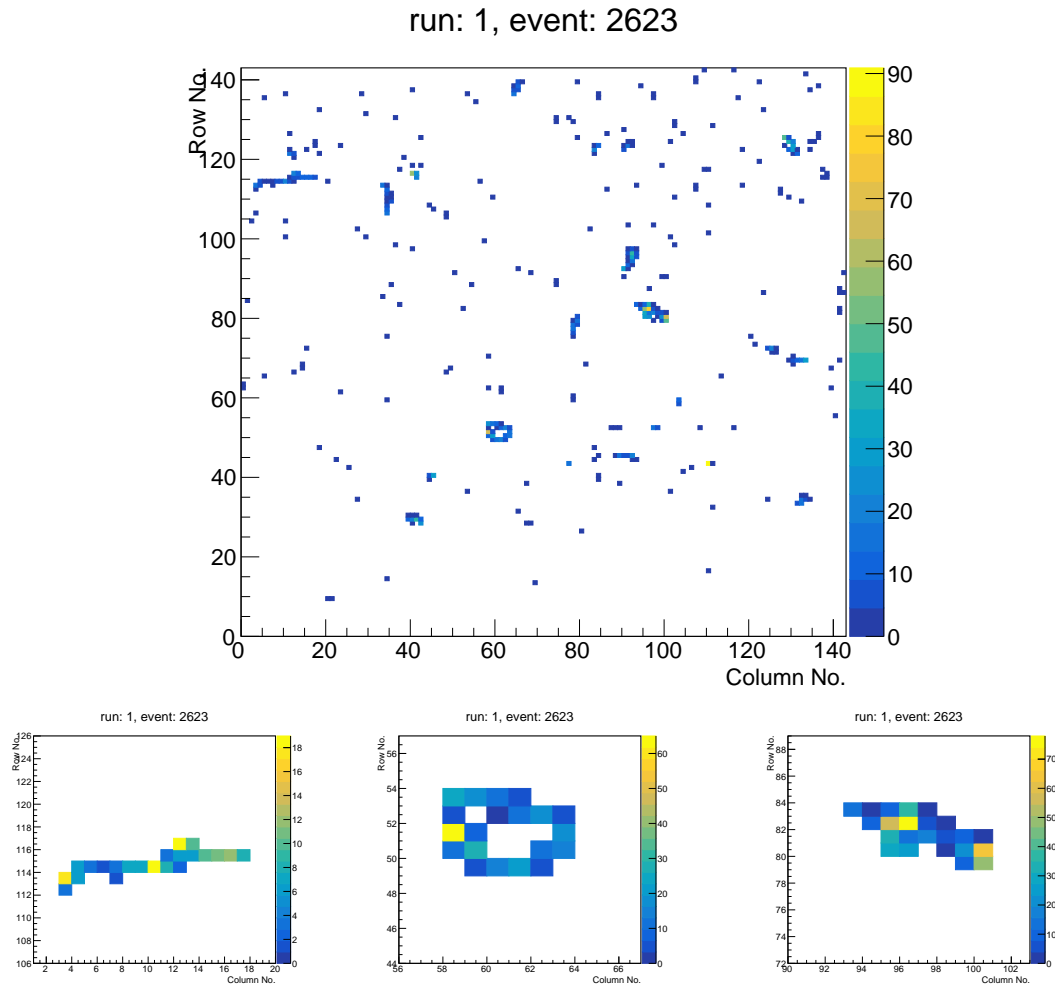


Figure 3.7: Image of β particles. The top figure is the all hit pixels and the below figures are the some of clustered events of this frame.

to across the plural pixels but only the partial energy deposited and escaped from the sensor may leave slightly longer track. There may be room to distinguish these events from the low energy photons.

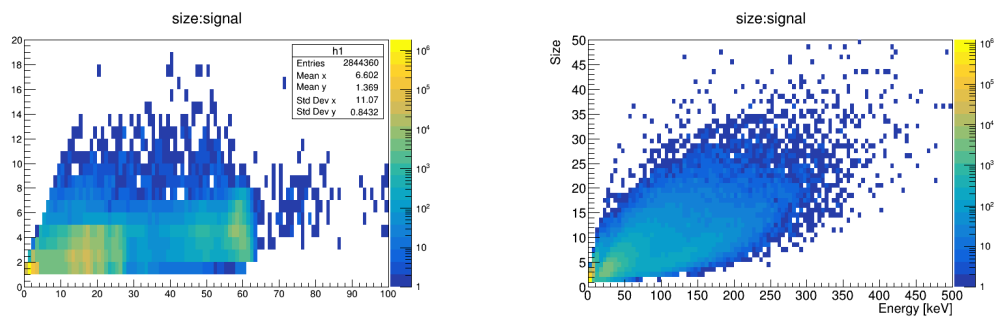


Figure 3.8: Dependence of the size of clusters and the total energy. The left side shows the γ -rays from Americium–241 and the right side shows the β particles from Strontium–90.

3.3 Background Measurement

The trial background measurement was performed to check the analysis flow and the feasibility of long-term measurement using XRPIX. This measurement was divided into three times as it shown in Table 3.1.

No.	Date	Experimental Time [h]	Live Time [h]
1	2017/6/9–2017/6/12	69.2	32.4
2	2017/6/30–2017/7/3	70.3	33.4
3	2017/7/4–2017/7/5	29.2	13.8
Total		168.7	79.6

Table 3.1: Measurement Time

The frame readout mode was used. The integration time of a frame was fixed at 10 ms. No shields were implemented. The bias voltage was 180 V, which is the full depletion voltage. The temperature was kept to 223 K (-50°C) using the thermal chamber.

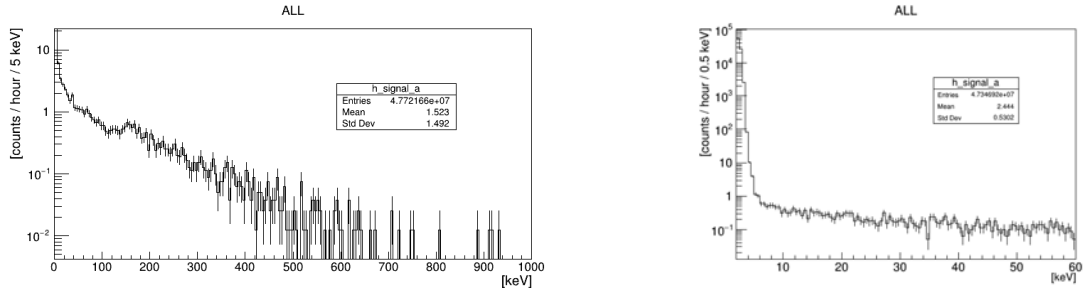


Figure 3.9: The result of background measurements. Left is the whole range and right is the low energy range.

The obtained spectrum is shown in Figure 3.9. Below 6 keV there remained a pedestal peak, caused by thermal noise. There is no obstructive peak around the axion signal 14.4 keV.

We can find a wide bump around 150 keV. This bump is thought to be mostly caused by cosmic muons. If muons pass through a silicon wafer, their energy loss is given by $dE/d(\rho x) \sim 2 \text{ MeVcm}^2/\text{g}$, where ρ is the density of silicon. Using $\rho = 2.3 \text{ g cm}^{-3}$ and the path length $x = 0.3 \text{ mm}$, the deposited energy is estimated to be about 150 keV.

If muons pass, they left linear tracks on the pixel detector. Then, the track-linearity test was investigated for the clusters which size was bigger than 10. As the test parameter of the linearity, a reduced chi-square χ^2/ν is used. First, for the position of pixels contained by a cluster (row, column) = (x, y) , a linear function $y = ax + b$ is fitted. ν is

the number of degrees of freedom of this fitting. The chi-square is defined as

$$\chi^2 = \sum_i^n \frac{d_i^2}{\sigma^2} \quad (3.1)$$

$$d_i = \frac{y_i - a_i x_i + b_i}{\sqrt{a_i^2 + 1}}, \quad (3.2)$$

where p_i means the parameter p of the i -th pixel, σ is the position resolution and in this case $\sigma = 1/\sqrt{6}$. The result is shown in Figure 3.10 and we see that events around 150 keV are concentrated in the region of $\chi^2/\nu \sim 1$.

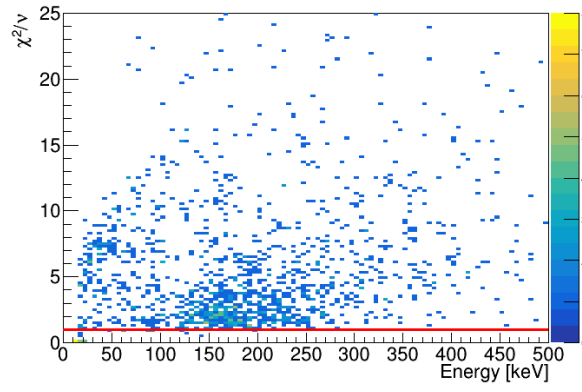


Figure 3.10: The scatter plot of χ^2/ν and energy. The red line shows $\chi^2/\nu = 1$.

This is an easy example of analytical background rejection using clustering information. It shows the availability of clustering for background study.

This measurement might mix many radiation sources but failed to distinguish them because of the poor statistic. The wide-area sensor is needed to study background in more detail and evaluate the sensitivity of the axion signal. That is why the XRPIX5 and stacking system are expected to give a great performance.

Chapter 4

Detector Background Simulation

Since the setup for the pilot experiment (mentioned in Section 2.3) is being developed now and not ready for measurements, the sensitivity estimation of the pilot experiment uses a detector simulation. Before the sensitivity estimation, the simulation is discussed in this chapter.

4.1 Simulation Scheme

There are some assumptions to simulate the experiment. To estimate the sensitivity, we need background information particularly, so the background simulation was done. Background events are roughly divided into two types, an external one and an internal one. The external events means cosmic rays muons and environmental radioactivity, and the secondary particles caused by them. This is thought to be mostly removable using the shielding and the VETO scintillation counters. The internal events means radioactive sources contained in the setup components. Some of them can be removable using anti-coincidence if the sequential decay occurs in a shorter time than the integration time and hits some of the sensors. For the present, the simulation does not consider the external background and focuses on the internal one. The VETO rejections are neither considered.

In this simulation, the structure of the sensor is not a form of pixel. The obtained data is the deposited energy in the sensor. The clustering analysis cannot apply to this simulation data and the discrimination between photons and electrons is not considered. These setting seems not to be a major factor to cause the big different result.

4.2 Chip Board Components

The image of the chip board is shown in Figure 4.1. The chip board is composed of a G10 circuit board, FPC connectors, an instrumentation amplifier, a potentiometer, ferrite

beads, ElectroMagnetic Interference (EMI) filters, Multi-Layered Ceramic Capacitors (MLCCs) and resistors. The list of the number of components is shown in Table 4.1.

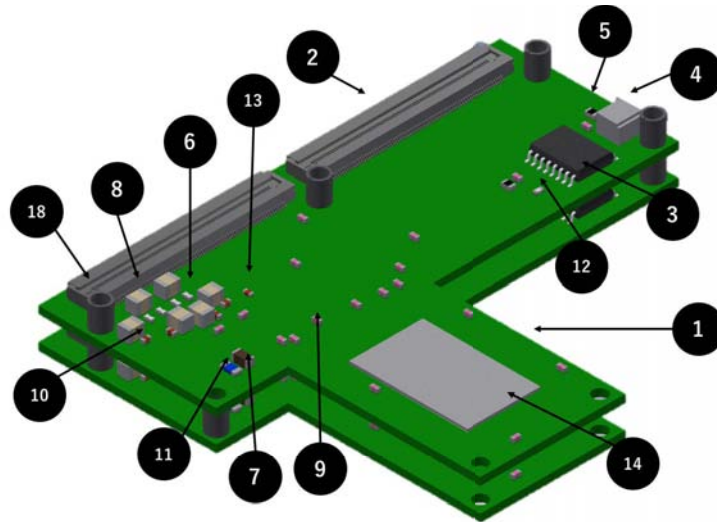


Figure 4.1: The schematic drawing of the chip board. The numbers in the figure correspond to Table 4.1

The material of the G10 circuit board is glass and epoxy resins. Epoxy resins are among the most versatile and widely used plastics in the electronics field, primarily because water absorption is virtually null, rendering it an outstanding insulator.

The radioactive measurement of these components was done using a High Purity Germanium (HPGe) detector, which is located on the second basement floor of Building No.1 of Faculty of Science, the University of Tokyo. In this measurement, amounts of ^{238}U series, ^{232}Th series and ^{40}K were estimated from detected γ -rays emitted from them. The detail of analysis is shown in Appendix B.

The result of the measurement is shown in Table 4.2. According to this result, the G10 board possesses the largest amount of radioactive sources among the components. The other components' radioactivity is small enough to be ignored. In the G10 board, ^{232}Th is the most abundant among the three impurities. The amount of radioactivity in the SOI chip is consistent with zero.

No.	Category	Quantity [per board]
1	G10 chipboard	1(16.4g)
2	Connector	2
3	Instru. Amp.	1
4	Potentiometer	1
5	Ferrite beads	2
6	EMI filter	4
7	0.047uF MLCC	1
8	100uF MLCC	6
9	0.1uF MLCC	19
10	10uF MLCC	4
11	10k Ω Resistor	1
12	6k Ω Resistor	1
13	10k Ω Resistor	1
14	XRPIX5b	1
15	Ag paste	
16	Pb free solder	
17	Pb/Sn solder	
18	Spacer	7

Table 4.1: The list of components of XRPIX5 chip boards.

No.	Category	Live Time [sec]	$^{238}\text{U}(^{214}\text{Pb})$ [mBq/board]	$^{238}\text{U}(^{214}\text{Bi})$ [mBq/board]	$^{232}\text{Th}(^{208}\text{Tl})$ [mBq/board]	^{40}K [mBq/board]
1	G10 chipboard	450000	851 ± 33	861 ± 38	$(1.55 \pm 0.06) \times 10^3$	$(1.18 \pm 0.15) \times 10^3$
2	Connector	600000	5.46 ± 0.32	4.48 ± 0.30	4.26 ± 0.40	3.82 ± 1.12
3	Instru. Amp.	510000	0.14 ± 0.28	-0.02 ± 0.24	-0.03 ± 0.38	-1.8 ± 1.2
4	Potentiometer	510000	0.32 ± 0.30	-0.07 ± 0.24	0.59 ± 0.40	1.4 ± 1.3
5	Ferrite beads	510000	0.038 ± 0.024	0.000 ± 0.020	0.084 ± 0.032	-0.02 ± 0.10
6	EMI filter	600000	0.436 ± 0.056	0.388 ± 0.048	-0.056 ± 0.064	-0.52 ± 0.20
7	0.047uF MLCC	660000	1.29 ± 0.02	1.24 ± 0.03	0.031 ± 0.017	-0.05 ± 0.05
8	100uF MLCC	150000	38.3 ± 0.60	33.6 ± 0.60	0.540 ± 0.258	-0.24 ± 0.72
9	0.1uF MLCC	600000	2.57 ± 0.27	1.58 ± 0.023	0.028 ± 0.018	-0.04 ± 0.05
10	10uF MLCC	390000	0.308 ± 0.060	0.328 ± 0.052	0.112 ± 0.076	-0.12 ± 0.20
11	10kΩ Resistor	600000	0.010 ± 0.011	0.004 ± 0.009	0.020 ± 0.015	-0.03 ± 0.05
12	6kΩ Resistor	600000	-0.004 ± 0.011	0.016 ± 0.010	-0.017 ± 0.014	-0.06 ± 0.04
13	10kΩ Resistor	600000	0.005 ± 0.011	0.003 ± 0.009	0.008 ± 0.014	-0.01 ± 0.05
14	SOI chip [1g]	750000	-0.139 ± 0.096	-0.103 ± 0.090	-0.015 ± 0.153	-0.27 ± 0.45
15	Ag paste [1g]	930000	-0.014 ± 0.114	-0.049 ± 0.098	0.06 ± 0.16	-0.86 ± 0.48
16	Pb free solder [1g]	510000	0.003 ± 0.043	-0.014 ± 0.037	-0.002 ± 0.058	-0.01 ± 0.20
17	Pb/Sn solder [1g]	600000	-0.074 ± 0.073	0.021 ± 0.066	-0.01 ± 0.10	0.13 ± 0.34
18	Spacer	—	—	—	—	—

Table 4.2: The result of the amount of radioactive matters contained by the components. SMK3-5(spacer) has not measured.

4.3 Geant4 MC Simulation

Geant4 is the simulation toolkit for radioactive experiments [27]. The supplementations of Geant4 is shown in Appendix C. Monte Carlo (MC) simulation means the method in which events are made probabilistically using random values. The kind of radioactive impurities and their amount in the chip board is shown in the previous section. Now, an energy spectrum of the background in the detector which is caused by the radioactive impurities can be estimated by the decay simulation at the position of the components. In this study, the radioactivity caused by the G10 board was simulated because it seemed to contribute to the background events the most among the components.

4.3.1 Detector Setup

In this simulation, the detector setup was defined as the composition of the below;

- ^ two chip boards
- ^ a ^{57}Fe foil ($32 \times 32 \times 0.04 \text{ mm}^3$)
- ^ a foil folder
- ^ OFHC shieldings and screws
- ^ lead blocks

and the image is just like the bottom right of Figure 2.7. Only the bottom sensor was made sensitive. There is a non-sensitive area around the sensitive area in the silicon sensor and the sensitive area in the simulation was defined as a $13.8 \times 21.9 \times 0.310 \text{ mm}^3$ box in the center of the whole chip, a $15.3 \times 24.6 \times 0.338 \text{ mm}^3$ box. The dimension of sensor is shown in Figure 4.2. The dimension and location of the other components was also defined as same as that of the real ones.

4.3.2 Particle Generation

The nucleus was placed in a random position in a volume of the component with no momentum. The ^{238}U and the ^{232}Th decays consecutively through the ^{238}U series and the ^{232}Th series to the stable lead, respectively. The decay chains of the ^{238}U series and the ^{232}Th series are shown in Figure 4.3 and 4.4, respectively. The ^{40}K decays once. The decay scheme is shown in Figure 4.5. The number of particles was calculated from the radioactivity measured by the HPGe detector. The number of emitting events is shown in Table 4.3.

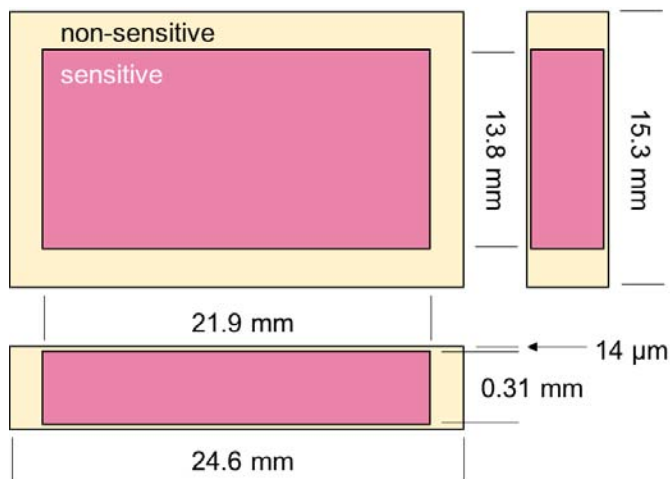


Figure 4.2: The dimension of the sensor.

	G10 board
Live time	1 month
^{238}U Emitting events	4.46×10^6
^{232}Th Emitting events	8.05×10^6
^{40}K Emitting events	6.10×10^6

Table 4.3: The number of simulated events

4.3.3 Result

Energy spectra are shown in Figure 4.6. The left figure shows the whole spectrum and the right one shows a lower energy region which contains the signal position, 14.4 keV.

There is a wide peak around 140 keV, which seems to be caused by high energy β particles produced from radioactive impurities. The characteristic X-ray of silicon ($K\alpha$: 1.74 keV), iron ($K\alpha$: 6.40 keV, $K\beta$: 7.06 keV) and copper ($K\alpha$: 8.04 keV, $K\beta$: 8.90 keV) can be seen clearly. There is another peak in 13.5 keV and this peak is caused almost from ^{228}Ra decays, contained by the ^{232}Th series. Besides this, no peak appeared and the background seems to follow a flat distribution. The event rate in the region $10 < E < 20$ keV is $1.36 \times 10^{-3} \text{ s}^{-1}$.

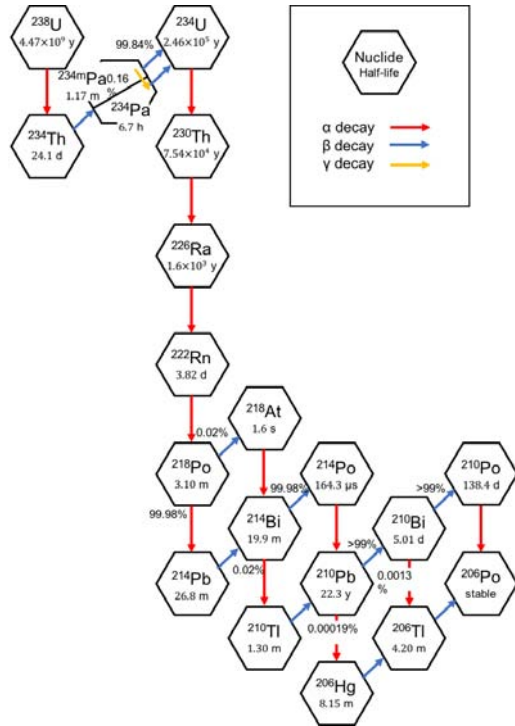


Figure 4.3: The ^{238}U series.

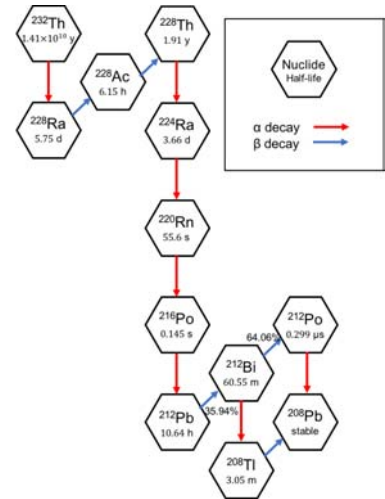


Figure 4.4: The ^{232}Th series.

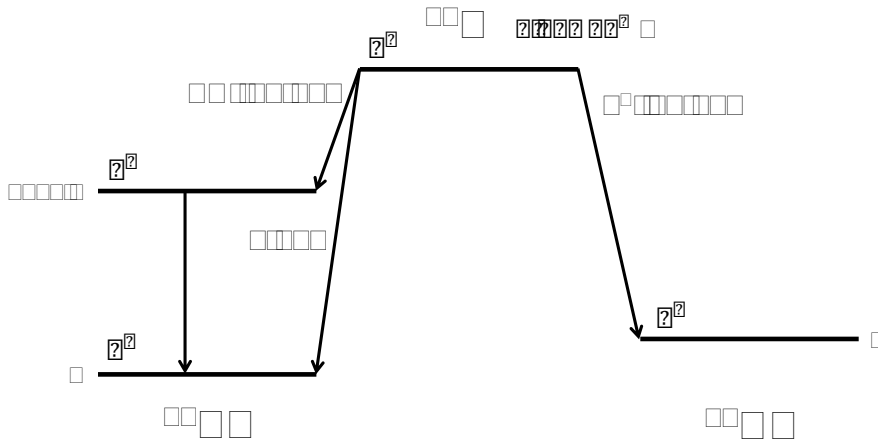


Figure 4.5: The decay scheme of ^{40}K .

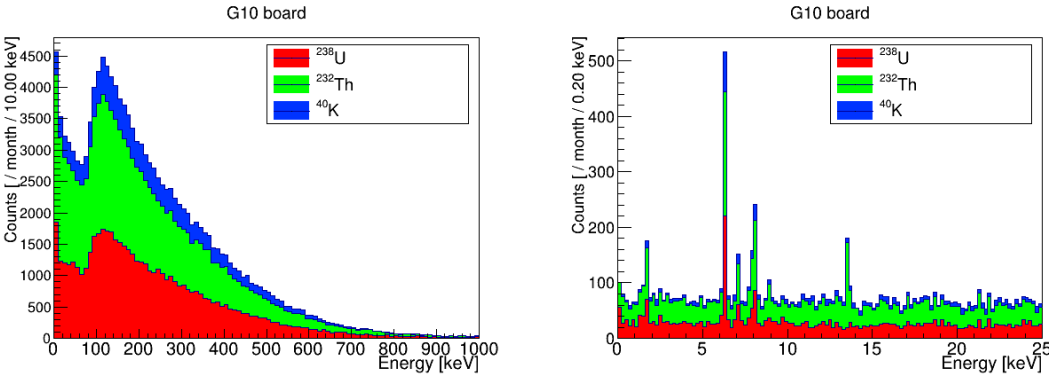


Figure 4.6: The result of G10: Energy spectra.

Chapter 5

Sensitivity Estimation

In this chapter, we discuss the sensitivity of the experiment with the obtained simulation data. Section 5.1 values a detection efficiency of γ -ray emitted from iron foil. Section 5.2 shows the method of evaluating the number of signal events and the limit estimation and Section 5.3 translates the number of events into the value of the axion mass.

5.1 Detection Efficiency for 14.4 keV γ -ray

A detection efficiency was determined by Geant4 MC simulation. The detector setup was the same as in section 4.3. 14.4 keV γ -rays were at random points in the iron foil and set isotropic random directions. The number of events is one million. We simulated two situations; γ -rays entering the sensor from frontside and backside. Distances between the sensor and the foil were 3.30 mm in the case of frontside and 3.00 mm in the case of backside. The obtained result is shown in Table 5.1. The efficiency of the case of frontside is higher than the one of backside though the distance of the frontside case is longer. This is because the area of the iron foil is bigger than the sensor. It may look smaller than intuitive estimation from solid angle but this result contains an effect of attenuation in the iron foil.

Frontside	Backside
$2.18 \pm 0.01\%$	$2.01 \pm 0.01\%$

Table 5.1: Detection Efficiency of 14.4 keV γ -rays

5.2 Signal Fitting Test

We use the energy spectrum data obtained by the background simulation in Section 4.3 and considering the detector resolution using Monte Carlo simulation. The strategy

of this analysis is maximum likelihood method. In the maximum likelihood method, parameters $\theta = \theta_i$ which we want to estimate are defined as the values which give the maximum of likelihood $\mathcal{L}(\theta)$. The likelihood is defined as $\mathcal{L}(\theta) = P(\mathbf{x} | \theta)$, where \mathbf{x} are the measured quantities and $P(\mathbf{x} | \theta)$ means the probability for \mathbf{x} when θ is given.

5.2.1 Likelihood Function and the Best Fit

The analysis region is defined for $10 < E < 20$ keV. The likelihood fit is performed on events falling in this region. As explained in section 4.3.3, the peak originating from ^{228}Ra appears in this region. The events in the region are assumed to be classified into three types; from signal, from radium, and from other sources. Energy distributions of signal and radium events are regarded as Gaussians. The other events distributions approximated to the first degree polynomials. Probability density functions (PDFs) of them are shown in below,

$$s(E) = \frac{1}{\sqrt{2\pi}\sigma_s} \exp\left[-\frac{(E - E_s)^2}{2\sigma_s^2}\right] \quad (5.1)$$

$$r(E) = \frac{1}{\sqrt{2\pi}\sigma_r} \exp\left[-\frac{(E - E_r)^2}{2\sigma_r^2}\right] \quad (5.2)$$

$$c(E) = AE + B \quad (5.3)$$

The signal events correspond to $s(E)$, the radium events to $r(E)$, the other events to $c(E)$. E_s and E_r are the means of signal and radium peaks, corresponding to 14.41 and 13.52 keV. $\sigma_s = 0.173$ keV and $\sigma_r = 0.167$ keV are detector resolutions at the energy points. A and B are fitting parameters for the continuous part. $s(E)$ and $r(E)$ are normalized functions but $c(E)$ is not yet. Considering normalization,

$$\int_{10}^{20} c(E) dE = 150A + 10B = 1$$

$$B = -15A + \frac{1}{10}$$

$c(E)$ can be redefined as

$$c(E) = A(E - 15) + \frac{1}{10}. \quad (5.4)$$

The number of signal, radium, and other events, $(N_{sig}, N_{Ra}, N_{bg})$, is determined by fitting with extended maximum log-likelihood method. The likelihood function is thus defined as

$$\begin{aligned} & \mathcal{L}(N_{sig}, N_{Ra}, N_{bg}, A) \\ &= \frac{N^{N_{obs}} \exp(-N)}{N_{obs}!} \prod_{i=1}^{N_{obs}} \left(\frac{N_{sig}}{N} s(E_i) + \frac{N_{Ra}}{N} r(E_i) + \frac{N_{bg}}{N} c(A, E_i) \right), \end{aligned} \quad (5.5)$$

where E_i is the observed energy for the i -th event. $N = N_{sig} + N_{Ra} + N_{bg}$ is the total number of events and N_{obs} is the number of detected events in the analysis region. Since it is easier to work using logarithms, (5.5) is transformed to

$$\begin{aligned} & \ln \mathcal{L}(N_{sig}, N_{Ra}, N_{bg}, A) \\ &= N_{obs} \ln N - N + \sum_{i=1}^{N_{obs}} \left[\ln \frac{1}{N} \left(N_{sig} s(E_i) + N_{Ra} r(E_i) + N_{bg} c(A, E_i) \right) - \ln i \right] \end{aligned} \quad (5.6)$$

and the values of the parameters which maximize the log-likelihood are decided.

The fitting result is shown in Figure 5.1 and Table 5.2. The total events $N = 3.53 \pm 0.06 \times 10^3$ is consistent with the total observed events $N_{obs} = 3524$.

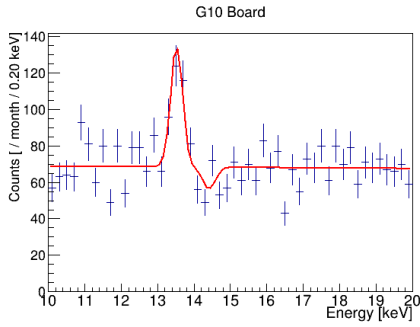


Figure 5.1: The result of fitting. The blue cross shows the simulation data and the red line shows the best fitted function.

Parameter	Value
N_{sig}	-25.4 ± 13.8
N_{Ra}	138 ± 19
N_{bg}	$(3.41 \pm 0.06) \times 10^3$
A	$(-0.19 \pm 0.60) \times 10^{-3}$

Table 5.2: The best values for the fit.

5.2.2 Confidence Interval

An upper limit of N_{sig} is considered. The other parameters, (N_{Ra}, N_{bg}, A) , are treated as nuisance parameters θ . The calculation is following the Feldman-Cousins approach [28] with profile construction [29]. As a test statistic, the *pro le likelihood ratio* is used. This is defined as the logarithm of the profile likelihood divided by its maximum value, like

$$q(N_{sig}) = -2 \ln \lambda_p(N_{sig}) \quad (5.7)$$

$$\lambda_p(N_{sig}) = \frac{\mathcal{L}(N_{sig}, \theta(N_{sig}))}{\mathcal{L}(N_{sig}, \theta)} \quad (5.8)$$

where N_{sig} and θ are the values of N_{sig}, θ which maximize the likelihood, $\theta(N_{sig})$ is the value which maximizes the likelihood for the specified N_{sig} . The values of N_{sig} and θ are given in Table 5.2. q as a function of N_{sig} is shown in Figure 5.2.

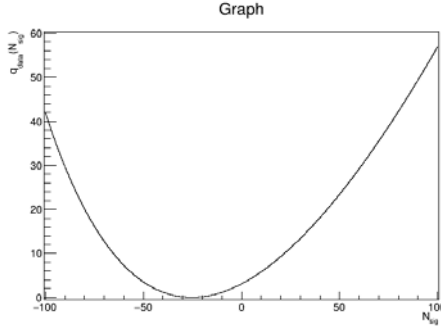


Figure 5.2: The parameter q as a function of N_{sig} . $q = 0$ when maximizing the likelihood.

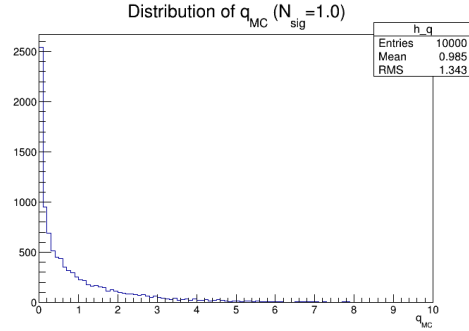


Figure 5.3: The distribution of $q_{MC}(1)$ generated by toy Monte Carlos.

Then, many pseudo data sets are generated from the Monte Carlo simulation. The number of events fluctuates following the Poisson distribution around the fixed N_{sig} , the best fit values of N_{Ra} and N_{bg} . The energy value for every event is generated by the PDF. For each MC data set, $q_{MC}(N_{sig})$ is calculated in the same way as (5.7).

The upper limit of N_{sig} at $1 - \alpha$ confidence level (C.L.) is defined as the N_{sig} where

$$q(N_{sig}) < q_{MC}(N_{sig}) \quad (5.9)$$

is satisfied in more than 100α % of the MC data sets. For example, the distribution of $q_{MC}(N_{sig} = 1)$ is shown in Figure 5.3. From Figure 5.2, we found $q(1) = 3.33$ and the ratio of $q_{MC}(1)$ which satisfies $q_{MC}(1) > 3.33$ is 0.067. Thus the C.L. of the upper limit $N_{sig} < 1$ is 0.933.

The C.L. for N_{sig} is shown Figure 5.4. The C.L. line exceeds 0.95 at the point $N_{sig} = 3$ for the first time. Interpolating a line connecting between the points of $N_{sig} = 2$ and $N_{sig} = 3$, the upper limit at 95% C.L., therefore, is found to be 2.8.

5.3 Mass Limit

As mentioned in Section 1.3, the mass of axion m_a can be determined by the rate of resonance axion absorption by the ^{57}Fe nucleus. For the counting rate R_a , the expected number of detected signal is

$$N_{sig} = \varepsilon \eta n_{57\text{Fe}} T R_a, \quad (5.10)$$

where ε is the detection efficiency, $\eta = 0.105$ is the fraction of gamma emission without internal conversion, $n_{57\text{Fe}}$ is the number of ^{57}Fe nuclei in the foil and T is the live time of the measurements. As shown in (1.38), the axion mass can be obtained as

$$m_a = 1.81 \times 10^8 \times \left(\frac{N_{sig}}{\varepsilon \eta n_{57\text{Fe}} (T/s)} \right)^{\frac{1}{4}} \text{ eV}. \quad (5.11)$$

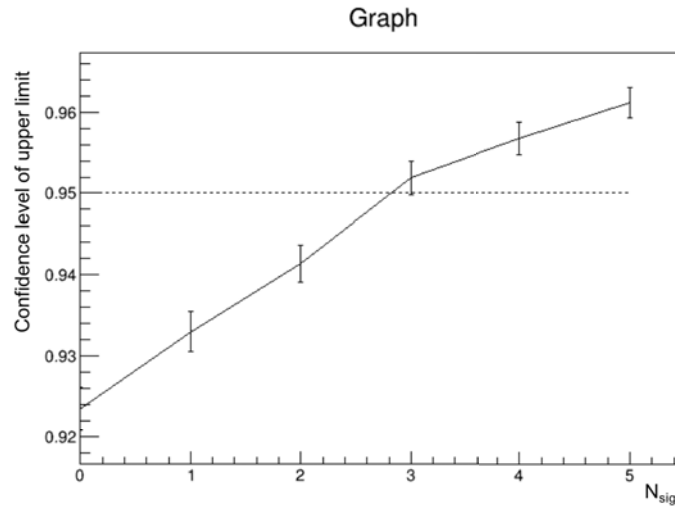


Figure 5.4: The confidence level for N_{sig} .

The case that only the bottom board is active is considered. From Section 5.1, the efficiency is employed as $\varepsilon = 2.18 \times 10^{-2}$. The number of ^{57}Fe nuclei contained by the foil is

$$n_{^{57}\text{Fe}} = \frac{N_A \rho_{\text{Fe}} V p}{M_{^{57}\text{Fe}}}, \quad (5.12)$$

where $N_A = 6.02 \times 10^{23} \text{ mol}^{-1}$ is Avogadro constant, $\rho_{\text{Fe}} = 7.87 \text{ g cm}^{-3}$ is the density of iron, $V = 0.41 \text{ cm}^3$ is the volume of the iron foil, $p = 0.959$ is the purity of ^{57}Fe in the foil, $M_{^{57}\text{Fe}} = 57 \text{ g mol}^{-1}$ is the atomic weight of ^{57}Fe . The live time is $T = 1 \text{ month} = 30 \times 24 \times 3600 \text{ s}$, set in Section 4.3.2. Using the result $N_{sig} < 2.8$, the upper limit of the axion mass is found to be $m_a < 113 \text{ eV}$.

Chapter 6

Discussion and Future Prospects

6.1 Estimations under Other Conditions

From the result of Chapter 5, we will extrapolate the sensitivity with taking account of some neglected effects. We use a naive approximation that, if the number of the observed events increases by a factor x , the error of the expected events increases by a factor about \sqrt{x} .

When both sensors are set active, the total events would be twice and the upper limit of the signal events would be found to $N_{sig} < 4.0$. The detection efficiency is 4.19% (see Table 5.1) and the amount of ^{57}Fe nuclei is not changed. Under this condition, the axion mass limit finds to $m_a < 104$ eV. This limit is the expected sensitivity of the pilot experiment configuration shown in Figure 2.7.

The live time was set to 30 days in the simulation. When the longer time is set, the lower upper limit we can obtained. The dependence of the live time is shown in Figure 6.1.

Only the internal background component was taken into account for the axion mass estimation in the previous chapter. Here, the external background is discussed. The total background rate measured in Section 3.3 was $(2.8 \pm 0.4) \times 10^{-2} \text{ h}^{-1} \text{ mm}^{-2} \text{ keV}^{-1}$, which is much larger than the internal background simulated in the previous chapter, $(1.62 \pm 0.03) \times 10^{-3} \text{ h}^{-1} \text{ mm}^{-2} \text{ keV}^{-1}$. Assuming almost all of the background event measured in Section 3.3 is the external background, we can estimate the background reduction by shielding. According to the result in Appendix A, the shielding of Pb 5 cm and Cu 6 mm carries a reduction by a factor of about 10 in the background events. If the background event rate measured in Section 3.3 reduces by the same factor of CdTe experiment, the external rate would be $2.8 \times 10^{-3} \text{ h}^{-1} \text{ mm}^{-2} \text{ keV}^{-1}$, which would be still larger than the internal one. According to Komura's report [30], Pb shielding can carry a reduction by a factor 100 ~ 200. If the external background succeeds in being reduced as much as this report, its rate would be at most $2.8 \times 10^{-4} \text{ h}^{-1} \text{ mm}^{-2} \text{ keV}^{-1}$, which

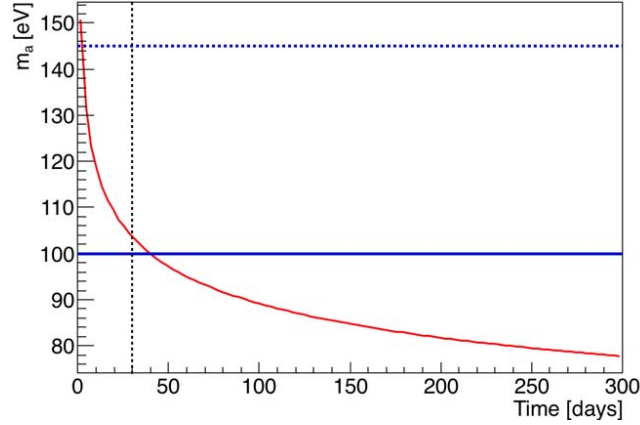


Figure 6.1: The live time dependence of the upper limits. The black dotted line shows the set time of this simulation. The blue solid line shows the current best limit of the axion mass using the axion-nucleon interactions and the dotted line shows the limit using ^{57}Fe , in particular.

would be smaller than the internal one. Under this condition, the external background would be negligible and the estimated upper limit would be realized.

If the VETO systems are introduced, the background event can be reduced more. For the internal background, the events that sequential decays occur and hit multiple sensors in a shorter time than the frame window can be rejected by using the frame coincidence of the XRPIX. The external events can be removed by using the scintillation counter as the cosmic muons trigger.

6.2 Comparison with Other Experiments

The recent result of experiments using the coupling between solar axion and nucleon is shown in Table 6.1. All limits use the parameter setting $S = 0.5$ and $z = 0.56$.

The current lowest limit using ^{57}Fe is $m_a < 145$ eV, which our pilot experiments could break, and, as shown in Figure 6.1, the increase of experimental time would break the lowest limit $m_a < 100$ eV. In order to obtain the sensitivity for lighter axion mass, more stacking chips, lower radioactive alternative parts and longer experiment time should be prepared.

Axion source; Energy, keV	Detection Reaction	Live Time, days	Upper Limit on m_a , eV (95% C.L.)	References
^{83}Kr ; 9.4	$A + ^{83}\text{Kr} \longrightarrow ^{83}\text{Kr}^*$	188.3	100	[31]
^{57}Fe ; 14.4	$A + ^{57}\text{Fe} \longrightarrow ^{57}\text{Fe}^*$	44.8	145	[19]
^{57}Fe ; 14.4	$A + ^{57}\text{Fe} \longrightarrow ^{57}\text{Fe}^*$	13.92	216	[32]
^{57}Fe ; 14.4	$A + ^{57}\text{Fe} \longrightarrow ^{57}\text{Fe}^*$	30	104	This simulating estimation

Table 6.1: Upper limits on the hadronic-axion mass from experiments devoted to searches for resonance axion absorption by ^{57}Fe and ^{83}Kr nuclei.

6.3 Developments for Low Background

For the main axion experiment, a low background chip board is planned to develop. In order to achieve the low background, the G10 board cannot be used and the alternative material is needed. As the candidate of this, a rigid-flexible printed circuits board is considered. The rigid flexible printed circuits board is composed by a rigid part like a G10 and a flexible part like an FPC. An sketch of the low background board is shown in Figure 6.2. The XRPIX chip is set on the FPC part and the G10 part is detached from the sensor part. Since bypass condensers must be placed near the chip, the components on the FPC part are only the chip and the capacitors which correspond to No.9 of Table 4.1.

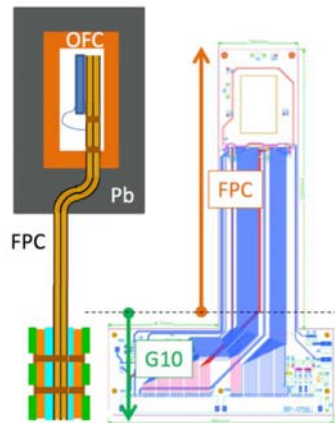


Figure 6.2: A schematic drawing of rigid flexible print circuits board

Here, the radioactivity caused by the 19 remained capacitors was simulated as the same setup as the G10 board. Though the configuration of the new setup differs from the setup of Section 2.3, this may be a good prediction. The time was changed to fifty years because the radioactivity of them is feeble so that the large statistic was needed.

Energy spectra are shown in Figure 6.3. Unlike the G10 board, the ^{238}U series is dominant. There is a 30 keV peak which did not appear in the spectrum of the G10 board. This peak seemed to be from characteristic X-rays of barium, which is contained by the ceramic capacitors. Since the effect of ^{232}Th series is not strong, the 13.5 keV peak did not appear. Compared with the G10 boards, the background rate in the analysis region is a factor of about 10^{-3} . It shows the new low background setup can be expected to obtain great sensitivity.

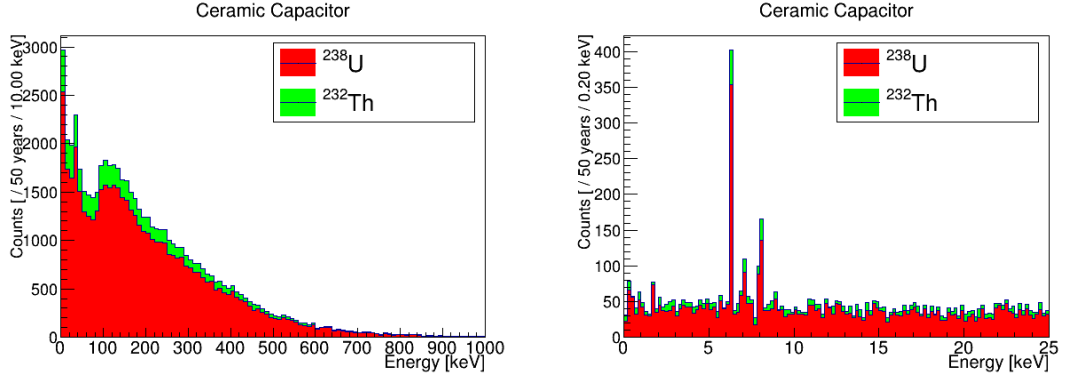


Figure 6.3: The result of Ceramic Capacitor: Energy spectra.

6.4 Goal of Axion Search

As mentioned in Section 1.3, the remained region is $10 \text{ eV} < m_a < 20 \text{ eV}$ and a final purpose is achieving the sensitivity for this region. Using (5.11), the required condition is

$$\frac{N_{sig}}{\varepsilon n_{57\text{Fe}} T} < 9.75 \times 10^{-31} \quad (6.1)$$

and the estimation of the pilot experiment corresponds to $N_{sig}/\varepsilon n_{57\text{Fe}} T = 1.52 \times 10^{-26}$, which means this parameter should be reduced by a factor of about 10^{-6} .

The effective plans are the increase of the amount of ^{57}Fe with keeping the detection efficiency and the reduction of the upper limits of the signal counts per a unit of time. What we should develop for this is a much lower background setup, a much higher energy resolution, a big-area XRPIX, stacking more XRPIX, increasing the acceptance of signal γ -rays and so on. For example, if a 100 times of detection area of sensor and enough iron foils are obtained and detection efficiency is not changed, N_{sig} would increase by a factor 10 and $n_{57\text{Fe}}$ could be set by a factor 100 thus the parameter $N_{sig}/\varepsilon n_{57\text{Fe}} T$ would come by a factor 10^{-1} . As shown in this example, not only one but all developments are required to achieve that goal.

Chapter 7

Conclusion

The sensitivity of the resonance absorption of 14.4 keV solar axion search has been estimated. We use XRPIX, the SOI pixel detector for X-ray, as the sensor of our experimental setup and checked the analysis method in the search for 14.4 keV X-rays, mainly the effectiveness of the clustering. The clustering is likely to distinguish γ -rays from other particles, α and cosmic muons, but difficult from low energy electrons. On the other hand, the VETO scintillation counters is expected to remove the second particle events caused by cosmic charged particles and the stack-XRPIX system is expected to remove the sequential decay events. These show the potential of the more reduction of the background event rate.

To estimate the sensitivity, the background events from internal parts were simulated using Monte Carlo methods. Although some minor conditions were neglected, this simulation would be reliable. The most radioactive component is the chip board itself, made of the G10 material which is known that much radioactive impurities are mixed. The expected rate of the events in the analysis region, $10 < E < 20$ keV, is $1.36 \times 10^{-3} \text{ s}^{-1}$ and there found obstructive peak caused by the ^{228}Ra decays, the part of the ^{232}Th series, at the point 13.52 keV.

The sensitivity of the pilot experiment was estimated by the extend maximum log-likelihood method and the Feldman-Cousins approach applying the simulated data. Introducing the PDFs of the energy discriminates the signal events from the ^{228}Ra decays events. The upper limit of axion mass when using one XRPIX is calculated as $m_a < 113 \text{ eV}$ ($S = 0.5, z = 0.56$) at 95% C.L. When using two XRPIXs, the limit is estimated as $m_a < 104 \text{ eV}$ at 95% C.L. This promises great performance compering with recent solar axion searches.

In order to obtain the sensitivity of more low mass, the low background setup is being developed. Since the G10 material is found to the big radioactive source, the alternative chip board is considered and it would make the background rate by a factor $\sim 10^{-3}$. Moreover, we need the larger statistics and the ultra-low-background setup for the “Hadronic Axion Window”.

References

- [1] C. A. Baker, D. D. Doyle, P. Geltenbort, K. Green, M. G. D. van der Grinten, P. G. Harris, P. Iaydjiev, S. N. Ivanov, D. J. R. May, J. M. Pendlebury, J. D. Richardson, D. Shiers, and K. F. Smith. Improved experimental limit on the electric dipole moment of the neutron. Phys. Rev. Lett., 97:131801, Sep 2006.
- [2] R. D. Peccei and Helen R. Quinn. CP Conservation in the Presence of Pseudoparticles. Phys. Rev. Lett., 38:1440–1443, June 1977.
- [3] Jihn E. Kim. Weak-interaction singlet and strong CP invariance. Phys. Rev. Lett., 43:103–107, July 1979.
- [4] M.A. Shifman, A.I. Vainshtein, and V.I. Zakharov. Can confinement ensure natural cp invariance of strong interactions? Nuclear Physics B, 166(3):493 – 506, 1980.
- [5] Michael Dine, Willy Fischler, and Mark Srednicki. A simple solution to the strong cp problem with a harmless axion. Physics Letters B, 104(3):199 – 202, 1981.
- [6] A. R. Zhitnitsky. On Possible Suppression of the Axion Hadron Interactions. (In Russian). Sov. J. Nucl. Phys., 31:260, 1980. [Yad. Fiz.31,497(1980)].
- [7] G. Rybka A. Ringwald, L.J. Rosenberg. Axions, Other Similar Particles, in Hypothetical Particles, Concepts, 2016.
- [8] A.C. Hayes J. Engel, D. Seckel. Emission and detectability of hadronic axions from SN 1987A. Phys. Rev. Lett., 65(8):960–963, 1990.
- [9] P. Sikivie. Experimental Tests of the “Invisible” Axion. Phys. Rev. Lett., 51, October 1983.
- [10] D. A. Dicus et al. Astrophysical bounds on the masses of axions and Higgs particles. Phys. Rev. D, 18:1829, 1978.
- [11] R. Ohta T. Mizumoto A. Yamamoto M. Minowa Y. Inoue, Y. Akimoto. Search of solar axions with mass around 1 eV using coherent conversion of axions into photons. Physics Letters B, 668:93–97, October 2008.

- [12] M. Arik et al. New solar axion search using the CERN Axion Solar Telescope with 4He filling. Physical Review D, 92, July 2015.
- [13] S. Moriyama. Proposal to Search for a Monochromatic Component of Solar Axions Using ^{57}Fe . Phys. Rev. Lett., 75(18), 1995.
- [14] K. Y. Lee W. C. Haxton. Phys. Rev. Lett., 66:2557, 1991.
- [15] K. Abe et al (E143 Collaboration). Phys. Rev. Lett., 75:25, 1995.
- [16] R. Mayle et al. Phys. Lett. B, 219:515, 1989.
- [17] D. Adams et al. Phys. Rev. D, 56:5330, 1997.
- [18] A. De Rujula and K. Zioutas. Phys. Lett. B, 217:354, 1989.
- [19] D. A. Semenov E. V. Unzhakov A. V. Derbin, V. N. Muratova. New limit on the mass of 14.4-keV solar axions emitted in an M1 transition in Fe-57 nuclei. Phys. Atom. Nucl., 74:620–626, 2011.
- [20] Y. Arai et al. Development of soi pixel process technology. Nuclear Instruments and Methods in Physics Research Section A: Accelerators, Spectrometers, Detectors and Associated Equipment, 636:S31–S36, April 2011.
- [21] A. Takeda et al. Design and Development of an Event-driven SOI Pixel Detector for X-ray Astronomy. In HSTD11/SOIPPIX2017, 2017.
- [22] A. Takeda et al. Design, Evaluation of an SOI Pixel Sensor for Trigger-Driven X-Ray Readout. IEEE Transactions on Nuclear Science, 60, April 2013.
- [23] Johny Alejandro Mora Grimaldo. Background Studies for Axion & WIMP Detection Experiments Using the XRPIX Silicon Detector. Master's thesis, The University of Tokyo, 2017.
- [24] J. Sander X. Xu M. Ester, H.P. Kriegel. A Density-Based Algorithm for Discovering Clusters in Large Spatial Databases with Noise. In 2nd International Conference on Knowledge Discovery, Data Mining, 1996.
- [25] J. Alejandro M. G. et al. Clustering & Tracking with a Single Event-Driven SOI Pixel Detector for Axion Search Experiment. In HSTD11/SOIPPIX2017, 2017.
- [26] M. Campbell et al. Charge collection from proton and alpha particle tracks in silicon pixel detector devices. In 2007 IEEE Nuclear Science Symposium Conference Record.

- [27] S. Agostinelli et al. GEANT4—a simulation toolkit. Nuclear Instruments and Methods in Physics Research A, 506, July 2003.
- [28] R. D. Cousins G. J. Feldman. Unified approach to the classical statistical analysis of small signals. Phys. Rev. D, 57(7):3873–3889, 1998.
- [29] C. Patrignani et al. (Particle Data Group). Chin. Phys. C, 40(100001), 2016 and 2017 update.
- [30] K. Komura. Present Status and Prospects of Ultralow Level Radioactivity Measurements (2), Underground Laboratory and Recent Topics Emerged from Ultralow Level Radioactivity Measurements. In RADIOISOTOPES, volume 55. Japan Radioisotope Association, May 2006.
- [31] Yu. M. Gavrilyuk et al. New experiment on search for the resonance absorption of solar axion emitted in the M1 transition of ^{83}Kr nuclei. JETP Lett., 101(10):664–669, 2015.
- [32] T. Namba. Results of a search for monochromatic solar axions using ^{57}Fe . Phys. Lett. B, 645:398–401, 2007.

Appendix A

Background Measurement using the CdTe Detector

The first background measurement was performed with the CdTe detector because the XRPIX was not available yet at that time. The setup of this measurement is shown in A.1. The information of the CdTe is shown in Table A.1. The detector and the preamplifier are in a box. The waveform shaping amplifier contains the power supply. The output of the ADC is digitized by 13 bit.

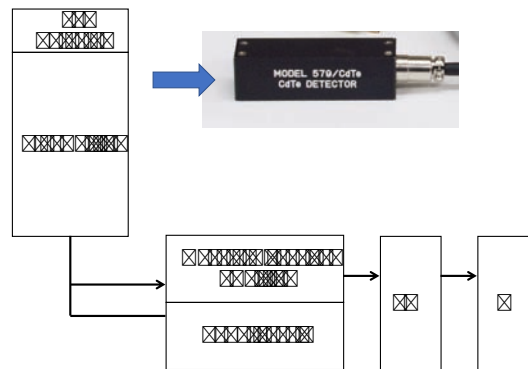


Figure A.1: The setup of the CdTe detector.

Characteristics	
Dimensions	$2 \times 2 \times 2_t$ mm
Resolution (FWHM)	2.5 ± 1.5 keV (at 60 keV)

Table A.1: Properties of the CdTe detector used in the first background measurements.

Four measurements were performed: one without any shielding (66 hours), one with only a 5 cm lead shielding with improved hermeticity (14 hours), one with a 5 cm lead

52 APPENDIX A. BACKGROUND MEASUREMENT USING THE CDTE DETECTOR

shield and a 6 mm copper shield (48 hours) and one with a 5 cm lead shield and a 12 mm copper shield, also with improved hermeticity (66 hours). The result is shown in Figure A.2. The total number of events between 13 keV – 16 keV for each measurement are shown in Table A.2.

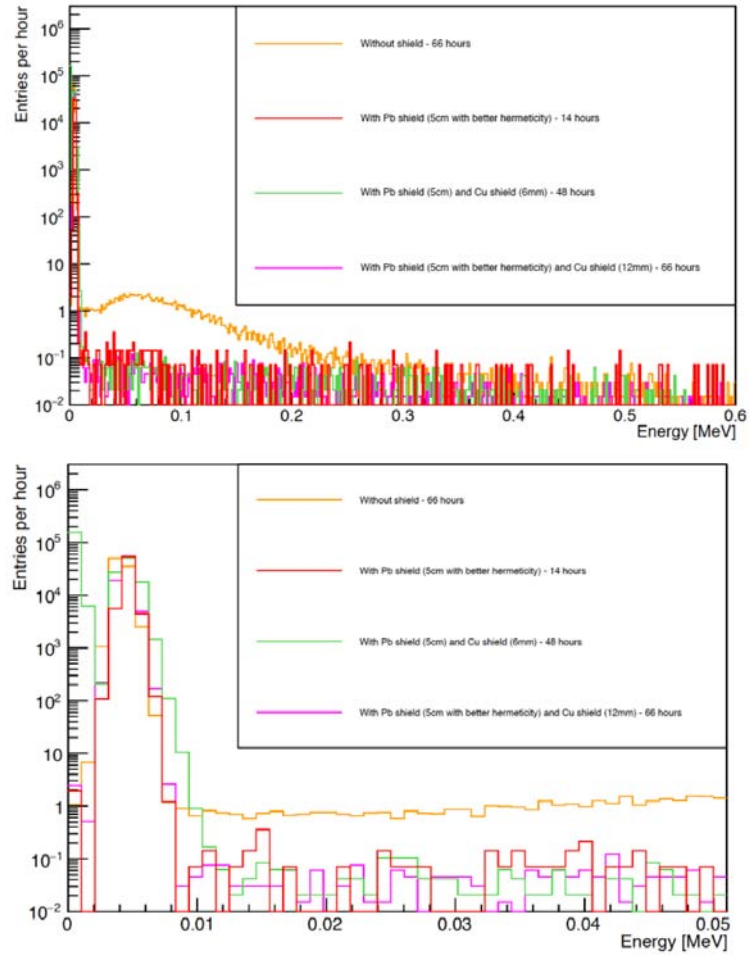


Figure A.2: Data taken with the CdTe detector

Measurement	Event rate [$\text{h}^{-1} \text{mm}^{-2} \text{keV}^{-1}$]
No shield	0.10985 ± 0.02039
Pb 5 cm	0.08929 ± 0.03993
Pb 5 cm & Cu 6 mm	0.01567 ± 0.00904
Pb 5 cm & Cu 12 mm	0.00757 ± 0.00535

Table A.2: Events rate for the four measurements performed, at 14.5 keV.

Appendix B

Analysis of Radioactive Impurity Data Taken with the HPGe

We used the HPGe detector in order to measure the number of radioactive sources contained in the chip board components. The three sources were measured, Uranium-238 series, Thorium-232 series, and Potassium-40. The number of observed events of each source is estimated by the fitting to the energy peaks. ^{238}U series was estimated using the 351 keV γ -rays from ^{214}Pb and the 609 keV from ^{214}Bi . ^{238}Th series was estimated using the 583 keV from ^{208}Tl . ^{40}K was estimated using the 1461 keV. The fitting function is a combination of a Gaussian and a first degree polynomials. The analysis uses three data; the components, the calibration stone, and the background. The calibration stone, which is abundant in radioactivity, is used to calibrate a scale of energy. The fitted mean and sigma are used for the component measurement as a constant value. The background means the data with no components. The fitted background events are subtracted to the fitted events of measured components. The fitting result of the SOI chip is show to Figure B.1.

The number of the sources is calculated from the obtained event number and the detection efficiency and the branching ratio. The detection efficiency differed with each component and was obtained by Geant4 simulation with monochromatic gamma ParticleGun.

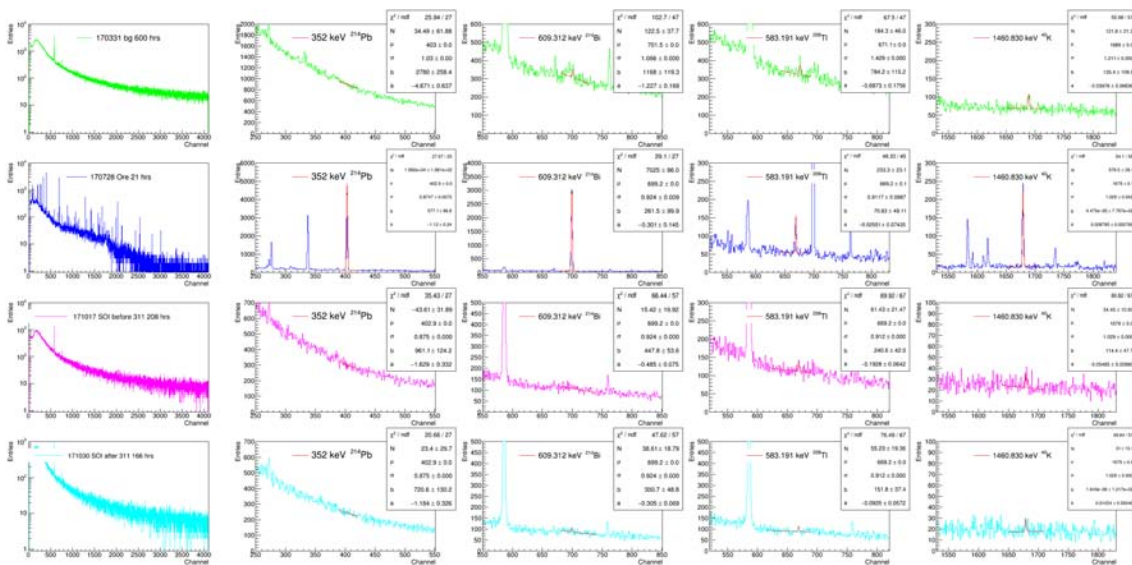


Figure B.1: The histograms of the measurement of SOI chip. The first row shows the BG run, the second shows the calibration run, the third and fourth shows the component measurements.

Appendix C

Geant4 Simulation Method

Geant4 is a toolkit for the simulation of the passage of the particles through materials. The base of the simulation is the Monte Carlo method. Geant4 simulates interactions of a radiative particle passing through matters successively.

In order to recreate sequential decays of ^{238}U and ^{232}Th in the simulation, we use G4RadioactiveDecay class which is prepared by Geant4. The G4RadioactiveDecay makes decays in conformity to Evaluated Nuclear Structure Data File (ENSDF), maintained by National Nuclear Data Center in Brookhaven National Laboratory.

Physical processes of the interactions are categorized into five parts, the electromagnetic interactions, the hadronic interactions, the optical processes, the decays and the transportations. In the electromagnetic process, the gamma interaction is selected from the photoelectric effect, the Compton scattering, the gamma conversion and the Rayleigh scattering. The charged particles interaction is selected from the multiple scattering, the ionization, and the bremsstrahlung. The fluorescences, the Auger electrons and the deexcitations of ions are considered in this process. As the electromagnetic interaction model, the Livermore library was used, which is the low energy electromagnetic interaction model. The hadronic interaction process contains the elastic and inelastic scattering, set for the alpha particles. In the optical processes, the scintillation and the optical photons are considered. The optical photons have two processes, the absorption and the boundary process. The decays mean the radioactive decays of nuclei.

The transportation setting has the step cutoff of the time and energy. The time cut is set only for the long-lived neutrons. The energy cut kills the very-low-energy charged particles.